ELECTRONIC MATERIALS

Surface conduction and reduced electrical resistivity in ultrathin noncrystalline NbP semimetal

Asir Intisar Khan[1], Akash Ramdas[2]†, Emily Lindgren[2,3]†, Hyun-Mi Kim[4]†, Byoungjun Won[5], Xiangjin Wu[1], Krishna Saraswat[1], Ching-Tzu Chen[6], Yuri Suzuki[3,7], Felipe H. da Jornada[2,8], Il-Kwon Oh[5]*, Eric Pop[1,2,7,9]*

The electrical resistivity of conventional metals such as copper is known to increase in thin films as a result of electron-surface scattering, thus limiting the performance of metals in nanoscale electronics. Here, we find an unusual reduction of resistivity with decreasing film thickness in niobium phosphide (NbP) semimetal deposited at relatively low temperatures of 400°C. In films thinner than 5 nanometers, the room temperature resistivity (~34 microhm centimeters for 1.5-nanometer-thick NbP) is up to six times lower than the resistivity of our bulk NbP films, and lower than conventional metals at similar thickness (typically about 100 microhm centimeters). The NbP films are not crystalline but display local nanocrystalline, short-range order within an amorphous matrix. Our analysis suggests that the lower effective resistivity is caused by conduction through surface channels, together with high surface carrier density and sufficiently good mobility as the film thickness is reduced. These results and the fundamental insights obtained here could enable ultrathin, low-resistivity wires for nanoelectronics beyond the limitations of conventional metals.

Ultrathin conductors with low electrical resistance are needed for hyperscaled nanoelectronics [1], from metal interconnects for dense logic and memory [2, 3] to neuromorphic [4] and spintronic devices [5, 6]. Low resistance allows lower voltage drops and lower signal delays, reducing power dissipation at the system level [7]. Resistance is proportional to resistivity, but the resistivity of conventional metals increases in films or wires thinner than the electron mean free path (few tens of nanometers at room temperature) because of electron-surface scattering [8]. For example, the room temperature resistivity of sub-5-nm thin Cu or Ru films is up to an order of magnitude larger than in bulk films (>100 nm) [8–10]. High electrical resistivity of ultrathin metals can be a key contributor to energy consumption in dense logic and memory [11, 12] and could ultimately limit the performance of future data-driven applications [4].

In this context, the topological Weyl semimetals NbP, NbAs, TaP, and TaAs [13–18] are promising because they could carry current within surface states that are topologically protected from disorder scattering [19]. The multifold fermion semimetals CoSi, RhSi, AlPt,

and GaPd have also been theoretically predicted [20, 21] to benefit from surface conduction with suppressed scattering [20]. In other words, as the thickness of such semimetals is reduced, the surface contribution to conduction [22] could lead to lower effective resistivity [12, 20, 23], whereas in conventional metals with nanoscale thickness, the electrons undergo more surface scattering [8, 11, 24]. For example, recent measurements of high-quality crystalline NbAs displayed more than an order of magnitude reduction in the effective resistivity of nanobelts, reaching ~2 μohm·cm for ~250-nm thickness compared with their bulk single-crystal value of ~35 μohm·cm [23] at room temperature.

Surface-dominated transport has also been recently reported in amorphous Bi_2Se_3 topological insulator films (>75-nm thick) without long-range order [25], and disordered Weyl semimetal WTe_x films [26] have shown good charge-to-spin conversion and electrical conductivity that are comparable to those of crystalline WTe_2 [27]. Such experimental demonstrations with amorphous topological insulators suggest the possibility of surface-state conduction in Weyl semimetals even in the absence of long-range order. However, it is not known whether disordered or noncrystalline semimetals in ultrathin films (i.e., sub-5 nm) maintain surface-dominated transport and could be used to realize low-resistivity materials beyond the limitations of conventional metals. Such noncrystalline semimetals are much more likely to be compatible with modern semiconductor processing and ultradense future electronics, in which limited thermal budgets (<500°C) pose challenges for depositing single-crystal materials.

In this work, we uncovered a reduction of electrical resistivity in noncrystalline NbP semi-

metal with decreasing thickness down to ~1.5 nm. We found lower effective resistivity in sub-5-nm thin NbP films compared with their bulk crystalline counterparts, which we attribute to a proportionally higher conduction through a surface channel in the ultrathin films.

Film growth and resistivity

The NbP films were sputtered on sapphire and other substrates at 400°C, a temperature compatible with back-end-of-line (BEOL) semiconductor fabrication [28]. As shown in Fig. 1A, a seed layer of Nb was used to reduce the lattice mismatch between the substrate and the NbP films [29] and to promote local short-range order, i.e., nanocrystallinity. All samples were capped in situ with a ~3- to 4-nm thick silicon nitride layer to limit surface oxidation (see the supplementary materials and methods, "materials deposition" section; fig. S1; and table S1). We used high-angle annular dark-field scanning transmission electron microscopy (HAADF-STEM) to image the cross section of the NbP/Nb thin films, revealing local short-range order and nanocrystallinity within an amorphous matrix in the NbP layer across various thicknesses (~18 nm in Fig. 1, B and C, and figs. S2 and S3 and ~1.5 to 4.3 nm in fig. S4). Energy-dispersive spectroscopy (EDS) and x-ray photoelectron spectroscopy (XPS) analysis confirmed the stoichiometry and the uniform distribution of Nb and P within our sputtered NbP samples (fig. S5). STEM, EDS, and XPS characterization methods are detailed in the supplementary materials and methods, "materials characterization" section.

We measured the in-plane electrical resistivity of our NbP/Nb films and control Nb samples using standard Hall and eddy current–based contactless methods [30] (for details, see the supplementary materials and methods, "device fabrication and electrical measurement" section). The control Nb samples were prepared with the same deposition conditions as the Nb seed layers beneath the NbP samples. Figure 1D shows that the measured total room temperature resistivity of NbP/Nb films decreased from ~200 μohm·cm for ~80-nm thick NbP to ~51 μohm·cm for ~1.5-nm thick NbP (all on 4-nm Nb). This resistivity plot includes the electrical and thickness contribution of the 4-nm seed Nb layer. However, the resistivity of our control Nb metal films increased substantially as their thickness was reduced over the same range.

The measured temperature dependence of total resistivity shown in fig. S6A revealed metallic behavior (resistivity proportional to temperature) in NbP films of 18 nm or thinner, here including the 4-nm Nb seed layer (shown separately in fig. S6B). By contrast, an ~80-nm NbP film (also on a 4-nm Nb seed) showed resistivity that was almost independent of temperature, a signature of disorder or impurity-dominated

[1]Department of Electrical Engineering, Stanford University, Stanford, CA, USA. [2]Department of Materials Science and Engineering, Stanford University, Stanford, CA, USA. [3]Geballe Laboratory for Advanced Materials, Stanford University, Stanford, CA, USA. [4]Korea Electronics Technology Institute, Seongnam-si, Republic of Korea. [5]Department of Intelligence Semiconductor Engineering, Ajou University, Suwon, Republic of Korea. [6]IBM T.J. Watson Research Center, Yorktown Heights, NY, USA. [7]Department of Applied Physics, Stanford University, Stanford, CA, USA. [8]Stanford Institute for Materials & Energy Sciences, SLAC National Accelerator Laboratory, Menlo Park, CA, USA. [9]Precourt Institute for Energy, Stanford University, Stanford, CA, USA.
*Corresponding author. Email: epop@stanford.edu (E.P.); ikoh@ajou.ac.kr (I.-K.O.)
†These authors contributed equally to this work.
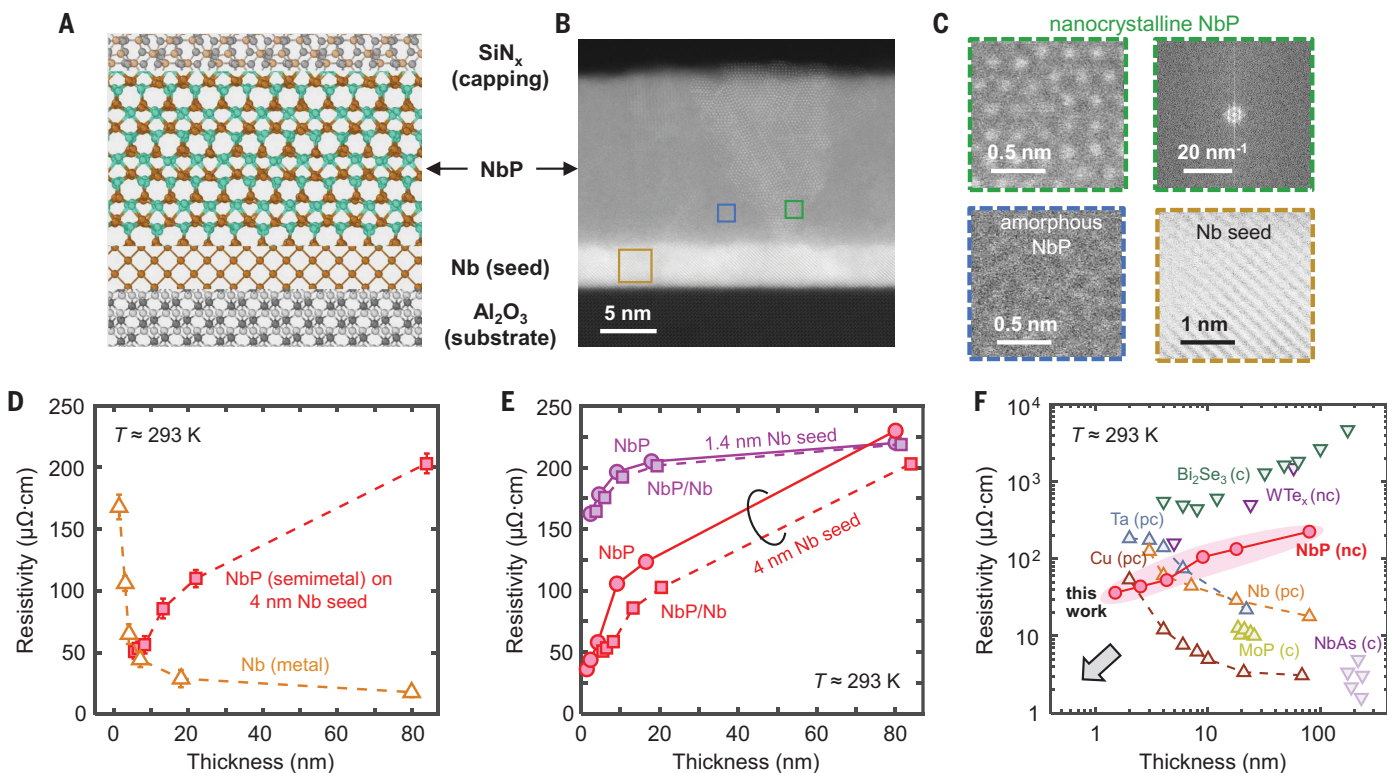
Fig. 1. NbP/Nb thin film stacks and room temperature resistivity.
(**A**) Schematic of the sputtered NbP/Nb film stack. (**B**) HAADF-STEM cross section of an ~18-nm NbP/Nb film stack. The Al_2O_3 substrate, thin (~4-nm) Nb seed layer, and silicon nitride capping can also be seen. (**C**) Magnified STEM images show local short-range ordering and nanocrystallinity within the amorphous NbP layer, as well as the crystallinity of the Nb seed layer (see fig. S2 for other NbP thicknesses). (**D**) Room temperature resistivity versus thickness of NbP/Nb films (squares) and control Nb films (triangles). The resistivity and thickness of NbP plotted here includes the 4-nm Nb seed layer. The NbP/Nb stack showed unconventional resistivity scaling in that the effective resistivity decreased in thinner films. Symbols and error bars mark the average and SD, respectively, across five samples of each film thickness. (**E**) Room temperature resistivity versus thickness of NbP/Nb stacks before (squares) and after (circles) subtracting the Nb seed-layer conduction contribution. Samples with two different Nb seed layers are shown: 4 nm (red) and 1.4 nm (violet). Unconventional resistivity scaling is noted for all films, both including and excluding the Nb seed layer contribution. The horizontal axis represents either the total stack thickness (NbP + Nb) or just the NbP thickness. (**F**) Room temperature resistivity versus thickness for various materials. Here, our sputtered NbP semimetal resistivity is shown after subtracting the contribution of the Nb seed; similarly, Cu resistivity is shown without the contribution of its liner and barrier layers (48). Other films include Nb (from this work); Ta; the crystalline topological insulator Bi_2Se_3 (32); the topological semimetals: noncrystalline WTe_x and crystalline NbAs (23, 26); and the topological metal MoP (45). The arrow marks the best corner region of smallest resistivity at low film thickness. c, pc, and nc (in parentheses) refer to crystalline, polycrystalline, and noncrystalline films, respectively. The sputtered NbP displayed decreasing resistivity down to sub-5-nm thickness, with the lowest resistivity in ultrathin films.

bulk states (25). The reduced effective resistivity of the thinner NbP films suggested that there may be a nonnegligible contribution from surface carriers to the total conductance of these samples (32, 33, 34), which is explored in more detail in Fig. 3.

Figure 1E shows that the unconventional resistivity scaling with thickness in our NbP/Nb film was preserved for varying thicknesses of the Nb seed layer (4 and 1.4 nm). This decreasing resistivity with decreasing film thickness was also observed after the conductance of the thin Nb seed layer (fig. S6C) was subtracted from that of the NbP/Nb stack (fig. S6D), indicating that the NbP film was responsible for the observed trend seen in Fig. 1E. For comparison, we also pre-pared Cu/Nb films with similar thickness; fig. S7 shows that their resistivity increased as their thickness was reduced both before and after subtracting the conductance contribution of the 4-nm Nb. In other words, the Nb layer did not influence the contrasting resistivity trend observed for NbP versus Cu. Figure 1E also shows that the resistivity of NbP on the 1.4-nm seed was higher than for NbP on the 4-nm Nb seed, which we attributed to the relatively lower strain in NbP with the thicker Nb seed, as discussed further below. The room temperature resistivity of our sub-3-nm thin NbP films on the 4-nm Nb seed was <45 μohm·cm, lower than the crystalline, bulk NbP resistivity of ~60 to 70 μohm·cm (14, 29). The thinnest, 1.5-nm NbP film reached 34 μohm·cm at room temperature

(red circles) after subtracting the Nb seed contribution. This is over six times lower than the bulk NbP resistivity in our thickest samples (Fig. 1E).

Figure 1F shows the scaling of room temperature resistivity versus thickness in our noncrystalline NbP semimetal, revealing a trend unlike traditional metals such as Cu, Nb, and Ta, and achieving one of the lowest resistivities at sub-5-nm thickness. We also quantify the total sheet resistance, $R_{\square}$, versus thickness of various films in fig. S8, including their seed or barrier layers, if any. As total thickness decreases from ~20 down to ~5 nm, the $R_{\square}$ of conventional metals increases by 10 to 100 times, but the $R_{\square}$ of topological semimetals increases by less than a factor of 2. Previously, resistivity smaller than the bulk resistivity was detected
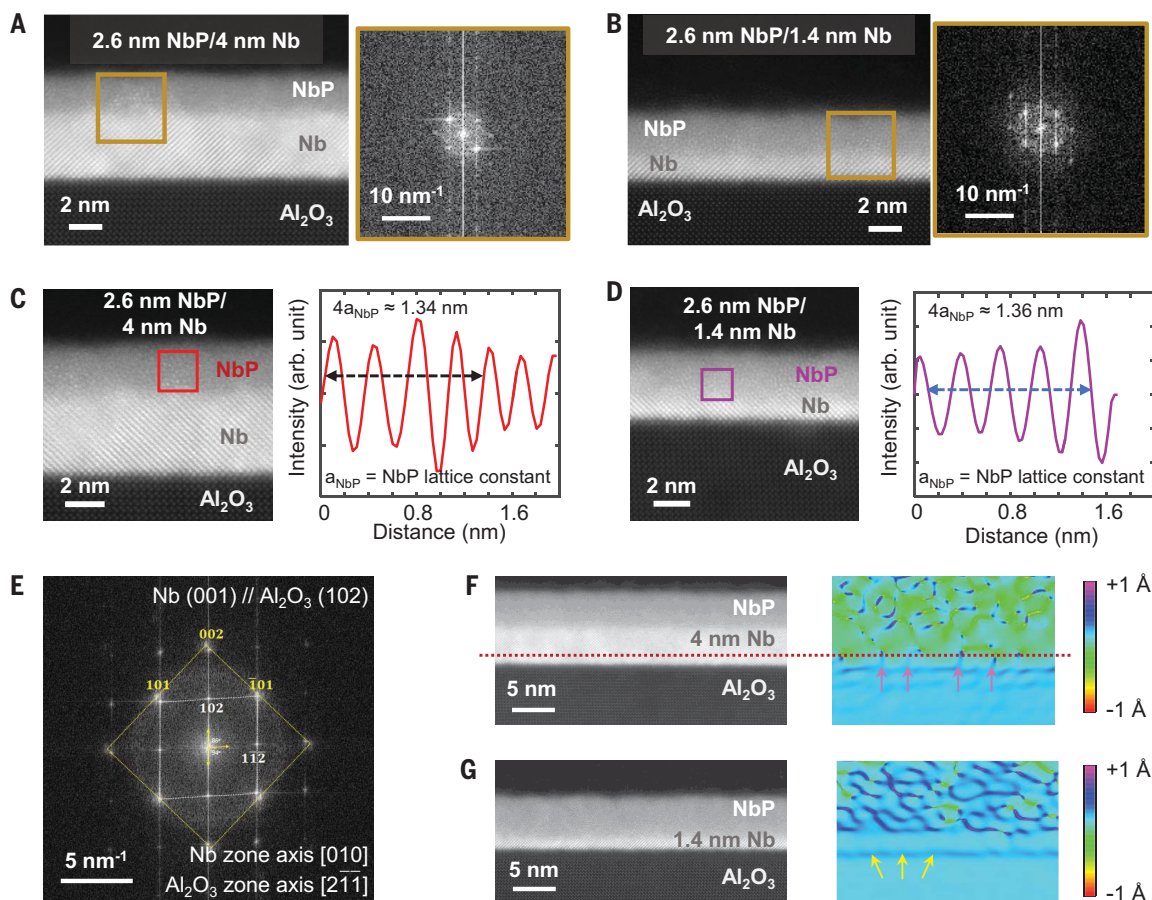
Fig. 2. Microstructure details of ultrathin NbP/Nb heterostructures.
(**A** and **B**) HAADF-STEM images and their fast Fourier transform (FFT) diffraction of 2.6-nm NbP films on Nb seed layer with 4-nm thickness (A) and 1.4-nm thickness (B). (**C**) Local nanocrystalline (short-range order) region of 2.6-nm thin NbP film on 4-nm Nb seed, showing a NbP lattice constant of ~3.34 Å, near its nominal value of ~3.332 Å (40). (**D**) Similar image on a 1.4-nm Nb seed layer, revealing a NbP lattice constant of ~3.41 Å, which indicated that NbP was strained on the thinner Nb seed. (**E**) Diffraction pattern of Nb seed layer and Al_2O_3 substrate. Nb seed layers have an epitaxial relationship with the Al_2O_3 substrate – Nb (001) || Al_2O_3 (102). The Al in Al_2O_3 (102) has a rhombus lattice tilted by 6° compared with Nb (001). (**F** and **G**) Lattice strain analysis of 2.6-nm NbP film on 4-nm Nb (F) and on 1.4-nm Nb (G) rom Fourier filtering the corresponding HAADF-STEM images. The 1.4-nm Nb seed was strained laterally along the Al_2O_3 surface (yellow arrows), but the accumulated strain was released in the 4-nm Nb seed by forming misfit dislocations (pink arrows). Red dotted line marks the level of dislocations within the Nb seed. The colored images display the strain mapping of the layers. The greater green proportion in the top plot marks a larger unstrained portion of NbP on the thicker (~4-nm) Nb seed compared with the thinner (~1.4-nm) one.

in NbAs nanobelts (23), topological insulators such as Bi_2Se_3 (32), and multifold fermion semimetal CoSi nanowires (35), although such films displayed greater crystallinity, greater thicknesses, and were deposited at higher temperature (typically >600°C). Multilayer graphene can also reach low resistivity in nanometer thin films, but only with substantial doping (36, 37) and with high-temperature growth and processing (38). By contrast, the low deposition temperature (400°C) of our noncrystalline NbP films is compatible with industrial BEOL processes, a key advantage for integration into state-of-the-art nanoelectronics (28, 39).

We also measured low resistivity and a similar resistivity scaling trend in ultrathin NbP films on different substrates such as MgO and SiO_2/Si (fig. S9A), as well as with different cap-

ping layers including silica and alumina. In terms of stability, uncapped NbP thin films (~2.6 nm) on 4-nm Nb measured in air showed a <10% change of resistivity after 4 days versus ~90% change in 4-nm Nb metal films, indicating less surface oxidation of NbP (fig. S9B). This stability is also promising for interconnect applications.

Structural studies

The resistivity of the sub-20-nm NbP thin films on 4-nm Nb seeds was notably lower than that of NbP on the 1.4-nm Nb seed. To understand this difference, we imaged ~2.6-nm thin NbP films on Nb seed layers with 4- and 1.4-nm thicknesses (Fig. 2, A and B, respectively) using atomic-resolution HAADF-STEM. Magnified STEM images and correspond-

ing diffraction patterns show the presence of similar nanocrystallinity within the amorphous matrices of NbP on both Nb seed layers (also see fig. S2 for 18-nm NbP films). Both 4- and 1.4-nm Nb seed layers were crystalline (fig. S3). NbP films were predominantly amorphous, with several nanometer-sized crystalline regions regardless of the Nb seed-layer thickness. Thus, the observed NbP resistivity scaling with thickness (Fig. 1E) for varying Nb seed layers would not likely be affected by the microstructure of the NbP films. The average lattice constant of our ~2.6-nm thin NbP film on the 4-nm Nb seed layer (Fig. 2C) was ~3.34 Å (~3.33 Å for ~18-nm NbP film; fig. S10A), near that of single-crystal NbP (40). However, Fig. 2D and fig. S10B show that the NbP film was strained, with higher average
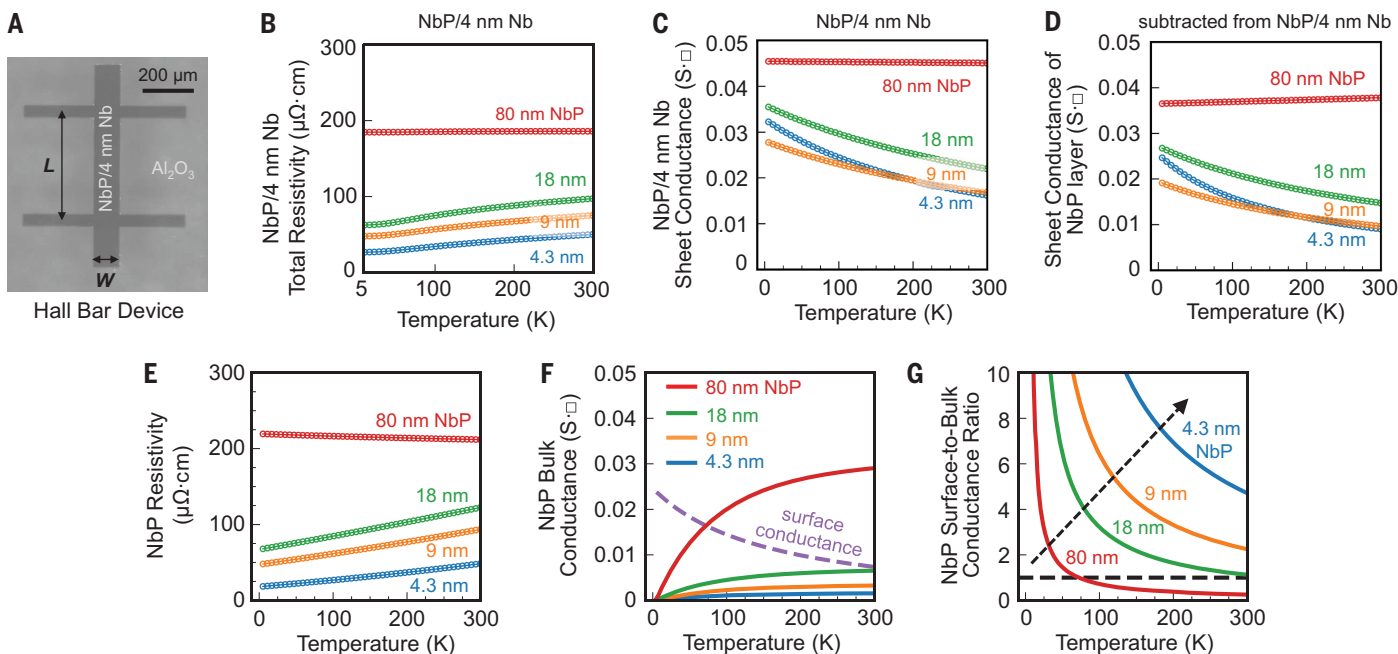
Fig. 3. Temperature-dependent transport of NbP/Nb and NbP. (**A**) Top view optical image of the Hall bar with width W of 100 μm and length L of 400 μm. The NbP was seeded by Nb and capped by SiN_x, as in Fig. 1B. (**B** and **C**) Temperature-dependent total resistivity of NbP/Nb (B) and sheet conductance of NbP/Nb films with varying NbP thicknesses (4.3, 9, 18, and 80 nm) on a 4-nm Nb seed (C). (**D**) Sheet conductance of the NbP layer of varying thicknesses obtained by subtracting the conductance of the 4-nm Nb seed layer (measured separately; see fig. S4A) from the total sheet conductance of NbP/Nb films in (C). (**E**) Temperature-dependent resistivity of NbP films with varying thicknesses, from 4.3 to 80 nm [obtained using (D)]. (**F**) Two-channel conductance fit to the resistivity data in (E), indicating a metallic surface channel conductance (dashed line) and disorder-dominated bulk conductance (solid lines). Here, we assumed the surface channel has zero thickness. Figure S13B displays the fit with a finite surface thickness of ~5 Å, yielding a similar result. (**G**) Calculated surface-to-bulk conductance ratio versus temperature for NbP films. The surface-to-bulk conductance ratio increased as the NbP film thickness was reduced (indicated by the dashed black arrow) across a wide range of temperatures. The region above the dashed line was dominated by surface conduction.

lattice constant (~3.41 Å for ~2.6-nm NbP and ~3.5 Å for ~18-nm NbP) on the 1.4-nm Nb seed layer, which could cause the higher resistivity (*41, 42*) seen for ultrathin NbP on the 1.4-nm Nb seed layer (Fig. 1E).

We further found (Fig. 2E) that the epitaxial relationship between the Nb seed and the Al_2O_3 substrate was Nb (001) || Al_2O_3 (102). The Al in Al_2O_3 (102) had a rhombus lattice tilted by 6° compared with the square lattice of the Nb (100) plane. As a result, in-plane misfit strain occurred between the Nb seed and the substrate (fig. S11). Increasing the Nb seed layer thickness generated misfit dislocations within the Nb that released this strain energy. We observed strain release in the films with ~4-nm Nb seed (Fig. 2F), where the Nb lattice returned to its cubic structure with nominal lattice constant of ~3.32 Å. For the thinner 1.4-nm Nb seed, the misfit dislocations that could release stress were not observed (Fig. 2G). This laterally strained the 1.4-nm Nb seed layer with a lattice constant of ~3.53 Å, near that of the Al_2O_3 substrate; therefore, the NbP films on the 1.4-nm Nb seed also display lateral strain (Fig. 2D and fig. S10B), and the strained NbP/Nb interface could also cause

charge scattering, further increasing the resistivity of the tensile NbP films (*41, 42*) on the 1.4-nm Nb seed (Fig. 1E).

Transport measurements

As our next step, we wished to understand what causes the unusual resistivity scaling trend (versus thickness) in our NbP semimetal films. Previous reports had suggested surface-dominated conduction in topological insulators (Bi_2Se_3) and topological semimetals (TaAs, NbAs) in both their crystalline (*23, 32, 33*) and amorphous or nanocrystalline Bi_2Se_3 (*25, 31*) films, attributed to topologically protected surface states. As the sample thickness decreases, conduction dominated by such surface states could explain the reduced resistivity of our thinner NbP films compared with their thicker counterparts. To understand this, we performed temperature-dependent transport measurements for a series of NbP thin films with varying thicknesses (~80 to ~4.3 nm) on the 4-nm Nb seed using standard Hall bar devices (Fig. 3A and see the supplementary materials and methods).

The unconventional trend of decreasing resistivity with decreasing NbP/Nb sample thickness persisted across all temperatures probed

down to 5 K (Fig. 3B). The three thinner NbP/Nb films (4.3-, 9-, and 18-nm NbP, each on 4-nm Nb) showed decreasing resistivity with decreasing temperature (metallic behavior). By contrast, the thick NbP/Nb film (~80-nm NbP on the 4-nm Nb seed) displayed a resistivity that was almost independent of temperature, a signature of disorder- or impurity-dominated bulk states (*25*). The reduced resistivity in the thinner NbP/Nb films that was maintained down to ~5 K suggested a non-negligible contribution of surface conduction in these samples (*32–34*).

To obtain the sheet conductance of the NbP layer (Fig. 3D), we subtracted the sheet conductance of the 4-nm Nb seed layer (fig. S6C) from the total sheet conductance of the NbP/Nb stack (Fig. 3C) over the 5 to 300 K temperature range. The extracted resistivity of the NbP layer also showed the unconventional trend of decreasing resistivity with decreasing NbP thicknesses from room temperature down to 5 K (Fig. 3E). To better understand the trend shown in Fig. 3E quantitatively, we fit the conductance of the NbP layers (with various thicknesses) with both bulk and surface channel contributions to the conductance
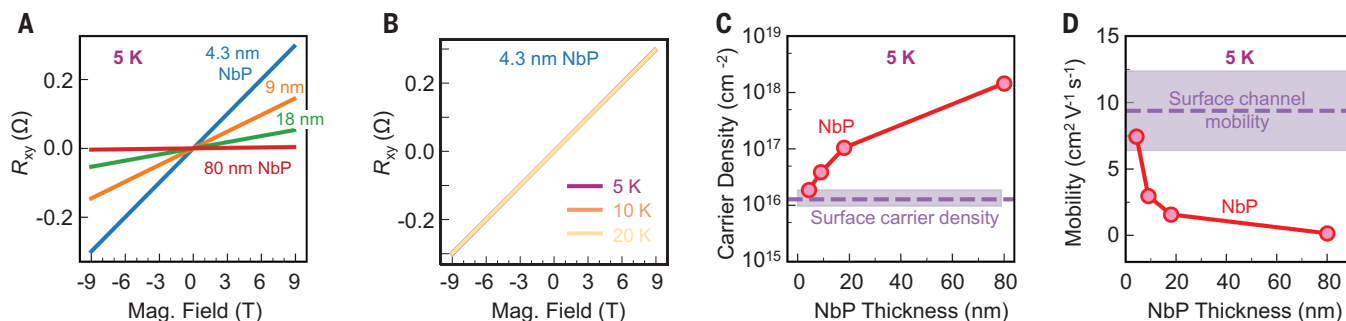
Fig. 4. Hall measurements and carrier densities of our NbP films. (**A**) Hall resistance versus magnetic field for NbP films with varying thicknesses at 5 K. (**B**) Hall resistance of a 4.3-nm thin NbP film versus magnetic field at 5, 10, and 20 K. (**C**) Sheet carrier density (holes, extracted from Fig. 4A) shows reduction with NbP film thickness. From the Hall coefficient versus thickness fit in fig. S17, we estimate a surface carrier density of $1.4 \pm 0.4 \times 10^{16}$ cm^{-2}, the sheet carrier density in the limit of zero NbP film thickness (shaded purple region). (**D**) Mobility of the NbP films showing an increasing trend with decreasing thicknesses. The shaded region represents the range of the surface channel mobility, 9.4 ± 3.0 cm^2 V^{-1} s^{-1}, estimated from the surface carrier density. All data and estimates in this figure were obtained after subtracting the conduction contribution of the 4-nm Nb seed (see the supplementary materials and methods and fig. S15). Including the conduction contribution of the 4-nm Nb seed layer did not alter the carrier density and mobility trends shown in (C) and (D) (fig. S18).

between 5 and 300 K (Fig. 3F and figs. S12 and S13). We assumed that the NbP surface conductance contribution was constant with the sample thickness (for further details, see the supplementary text, "surface and bulk conductance of NbP/Nb and NbP layer" section, and fig. S12).

As can be seen from Fig. 3F and fig. S13, the bulk conductance of our NbP films increased from 5 to 300 K, as would be expected for variable-range hopping behavior in amorphous and nanocrystalline films (25). Conversely, the surface conductance was metallic and decreased with increasing temperature (25, 32). As thickness decreased from ~80 to ~4.3 nm, the bulk contribution to the conductance decreased. At low temperatures, we expected the hopping carrier transport to be small and nearly independent of sample thickness. Thus, the conduction was dominated by a surface channel at low temperature (e.g., <50 K) even in the thicker 80-nm NbP sample (25, 32).

We also estimated the surface-to-bulk conductance ratio (Fig. 3G), which revealed that all of the thinner films (18-nm NbP or less) were dominated by their surface contribution up to room temperature. The resistivity of our 4.3-nm NbP film was smaller than the bulk single-crystal NbP resistivity (14, 29), whereas the resistivity of our 80-nm NbP film (Fig. 1E) was ~3× higher than the single-crystal value. The lower resistivity of our thinner NbP was unlikely to have been the result of improved crystallinity because these films were predominantly amorphous with embedded nanocrystallites (Fig. 2, A and B).

We also estimated the bulk NbP conductance and effective surface conductance of NbP (with the Nb layer) from the total sheet conductance of the NbP/Nb samples versus NbP thickness in fig. S14, with the analysis detailed in the supplementary materials and methods. Figure S14A shows that the surface conductance dominated the total sheet conductance for all NbP/Nb film stacks thinner than ~30 nm at room temperature. Even in the presence of defects or disorder, the higher conductivity in our thinner NbP/Nb films and NbP layers came from a surface-like channel.

Carrier density estimates

We performed Hall resistance measurements of our NbP films as a function of magnetic field at 5 K (Fig. 4A). We subtracted the deduced Hall conductivity of the 4-nm Nb seed layer (fig. S15A) from that obtained for our stacks (fig. S15B). As shown in Fig. 4A, the Hall resistance was linear with magnetic field at all sample thicknesses, suggesting that a single carrier dominated transport in our NbP films (in this case, holes). The Hall resistance of our 4.3-nm thick NbP versus magnetic field was nearly independent of temperature between 5 and 20 K (Fig. 4B). The extracted sheet carrier density at 5 K shown in Fig. 4C decreased from ~10^{18} cm^{-2} for 80-nm thick NbP to ~10^{16} cm^{-2} in 4.3-nm thin NbP (for details, see the supplementary text). This trend was consistent with previous reports on thicker films of the crystalline topological semimetals NbAs and TaAs (23, 33).

The carrier density per unit volume in our NbP films (>10^{22} cm^{-3}; fig. S16) was higher (43) than that in NbP bulk single crystals (14) but comparable to other topological semimetals such as ~70-nm thick NbP epitaxial films (>10^{22} cm^{-3}) (29), textured and amorphous CoSi (44), and topological metals such as MoP (>10^{23} cm^{-3}) (45). In addition, the effective carrier density estimated from Hall measurements in disordered or noncrystalline films, such as our NbP, could be overestimated (and the mobility underestimated) due to possible contribution from hopping-like transport (46). This has been reported in organic semiconductors (46) and the topological insulator Bi$_2$Se$_3$, where the total carrier density estimated in noncrystalline films was ~10 times higher (25) than in its crystalline counterpart (32).

The carrier density versus thickness trend (Fig. 4C) allowed us to estimate an average surface carrier density of ~10^{16} cm^{-2}, i.e., the hole density in the limit of the NbP film thickness approaching zero. This projected surface carrier density in our noncrystalline NbP was ~3 times larger than what was estimated in crystalline NbAs (23); however, it is consistent with the possibility of a higher apparent carrier density from Hall measurements in a noncrystalline system, as explained above.

The estimated mobility at 5 K (Fig. 4D) showed an increasing trend with decreasing NbP thickness. The effective mobility (at 5 K) of a 4.3-nm thin NbP film was ~7.4 cm^2 V^{-1} s^{-1}, ~50 times greater than that of the 80-nm thick NbP film (~0.15 cm^2 V^{-1} s^{-1}). Using the extrapolated surface sheet carrier density (Fig. 4C) and surface conductance (Fig. 3F), we estimated the mobility (see the supplementary text) of the surface-like channel to be 9.4 ± 3.0 cm^2 V^{-1} s^{-1}. This higher surface mobility appears to enable the lower resistivity in our thinnest NbP films (Fig. 3E), where conduction is dominated by surface rather than bulk channels (Fig. 3G). These estimates were performed after careful subtraction of the 4-nm Nb seed layer contribution (fig. S6); however, we found that the thickness-dependent carrier density and mobility trends shown in Fig. 4, C and D, were maintained even when the Nb layer is included, i.e., in NbP/Nb heterostructures (fig. S18).

What are the origins of the surface-like conduction in these ultrathin noncrystalline films?

This remains a partly open question, but we suggest a few possible causes. One possibility is the formation of disorder-tolerant Fermi arc–like surface states (23) even in noncrystalline topological materials (43, 47). Another cause may be the existence of an interfacial free-electron gas–like state (32) near the NbP/Nb interface, where we observed local short-range ordering (Fig. 2, A and B, and fig. S4). For example, topological surface states are expected to be metallic-like in nature (25) and less sensitive to disorder scattering (19, 23). The estimated surface mobility ($\sim$9.4 cm^2 V^{-1} s^{-1} at 5 K) of our noncrystalline NbP films was much lower than that of crystalline NbP ($\sim$10^6 cm^2 V^{-1} s^{-1} at $\sim$2 K) (14) and topological insulators such as Bi$_2$Se$_3$ ($\sim$10^3 cm^2 V^{-1} s^{-1} at 1.5 K) (32). However, the surface mobility in our films is comparable to mobilities found in sub-10-nm thin polycrystalline Bi$_2$Se$_3$ (<10 cm^2 V^{-1} s^{-1} at 1.5 K) (32, 34) and in thick amorphous Bi$_2$Se$_3$ (<20 cm^2 V^{-1} s^{-1} at 2 K) (25) with topological surface states. The low resistivity of our ultrathin NbP films was caused by the combination of high surface carrier density ($\sim$10^{16} cm^{-2}) and sufficiently good surface mobility. The low effective resistivity that we found was surface dominated and maintained up to room temperature in all sub-18-nm thin films (Fig. 3). Looking ahead, we expect our work to motivate future efforts into imaging surface-state dispersion in amorphous or noncrystalline semimetals, for example, by using surface-sensitive techniques such as angle-resolved photoemission spectroscopy (ARPES) and spin-resolved ARPES (25).

In conclusion, we found that the resistivity of noncrystalline NbP films decreased substantially as the film thickness was reduced, which is a trend counter to that observed in most common metals. The thinnest films (<5 nm) displayed resistivities lower than conventional metals of similar thickness at room temperature. Measurements and modeling indicated that our NbP films thinner than $\sim$18 nm were dominated by surface conduction up to room temperature, which is the origin of the effective resistivity decrease in thinner films. These films were deposited by large-area sputtering at relatively low temperatures (400°C) compatible with modern microelectronics processing. These results and the fundamental insights obtained here could enable ultrathin topological semimetals as low-resistivity interconnects in future high-density electronics.

REFERENCES AND NOTES

1. S. Salahuddin, K. Ni, S. Datta, *Nat. Electron.* **1**, 442–450 (2018).
2. A. A. Vyas, C. Zhou, C. Y. Yang, *IEEE Trans. Nanotechnol.* **17**, 4–10 (2018).
3. M. M. Shulaker et al., *Nature* **547**, 74–78 (2017).
4. D. Ielmini, H.-S. P. Wong, *Nat. Electron.* **1**, 333–343 (2018).
5. S. Jung et al., *Nature* **601**, 211–216 (2022).
6. L. Zhu et al., *Adv. Funct. Mater.* **29**, 1805822 (2019).
7. V. Huang, D. Shim, H. Simka, A. Naeemi, in *2020 IEEE International Electron Devices Meeting (IEDM)* (IEEE, 2020), pp. 32.6.1–32.6.4; https://doi.org/10.1109/IEDM13553.2020.9371945.
8. D. Gall, *J. Appl. Phys.* **127**, 050901 (2020).
9. E. V. Barnat, D. Nagakura, P.-I. Wang, T.-M. Lu, *J. Appl. Phys.* **91**, 1667–1672 (2002).
10. E. C. Ko, J. Y. Kim, H. Rhee, K. M. Kim, J. H. Han, *Mater. Sci. Semicond. Process.* **156**, 107258 (2023).
11. D. Gall, in *2020 International Symposium on VLSI Technology, Systems and Applications (VLSI-TSA)* (IEEE, 2020), pp. 112–113; https://doi.org/10.1109/VLSI-TSA48913.2020.9203700.
12. C.-T. Chen et al., in *2020 IEEE International Electron Devices Meeting (IEDM)* (IEEE, 2020), pp. 32.4.1–32.4.4; https://doi.org/10.1109/IEDM13553.2020.9371996.
13. N. P. Armitage, E. J. Mele, A. Vishwanath, *Rev. Mod. Phys.* **90**, 015001 (2018).
14. C. Shekhar et al., *Nat. Phys.* **11**, 645–649 (2015).
15. S.-Y. Xu et al., *Nat. Phys.* **11**, 748–754 (2015).
16. L. Rocchino et al., *Nat. Commun.* **15**, 710 (2024).
17. S.-Y. Xu et al., *Science* **349**, 613–617 (2015).
18. J. N. Nelson et al., *Matter* **6**, 2886–2899 (2023).
19. G. Resta, S.-T. Pi, X. Wan, S. Y. Savrasov, *Phys. Rev. B* **97**, 085142 (2018).
20. S.-W. Lien et al., *NPJ Quantum Mater.* **8**, 3 (2023).
21. N. B. M. Schröter et al., *Nat. Phys.* **15**, 759–765 (2019).
22. M. Breitkreiz, P. W. Brouwer, *Phys. Rev. Lett.* **123**, 066804 (2019).
23. C. Zhang et al., *Nat. Mater.* **18**, 482–488 (2019).
24. T. Zhou, D. Gall, *Phys. Rev. B* **97**, 165406 (2018).
25. P. Corbae et al., *Nat. Mater.* **22**, 200–206 (2023).
26. X. Li et al., *Matter* **4**, 1639–1653 (2021).
27. M. J. Mleczko et al., *ACS Nano* **10**, 7507–7514 (2016).
28. J. Schmitz, *Surf. Coat. Tech.* **343**, 83–88 (2018).
29. A. Bedoya-Pinto et al., *ACS Nano* **14**, 4405–4413 (2020).
30. J. Krupka, D. Nguyen, J. Mazierska, *Meas. Sci. Technol.* **22**, 085703 (2011).
31. L. He et al., *Nano Lett.* **12**, 1486–1490 (2012).
32. N. Bansal, Y. S. Kim, M. Brahlek, E. Edrey, S. Oh, *Phys. Rev. Lett.* **109**, 116804 (2012).
33. N. L. Nair et al., *Phys. Rev. B* **102**, 075402 (2020).
34. A. A. Taskin, S. Sasaki, K. Segawa, Y. Ando, *Phys. Rev. Lett.* **109**, 066803 (2012).
35. C.-I. Tsai et al., *Cryst. Growth Des.* **9**, 4514–4518 (2009).
36. J.-Z. Huang et al., *ACS Appl. Nano Mater.* **6**, 10680–10686 (2023).
37. J. Jiang, J. H. Chu, K. Banerjee, in *2018 IEEE International Electron Devices Meeting (IEDM)* (IEEE, 2018), pp. 34.5.1–34.5.4; https://doi.org/10.1109/IEDM.2018.8614535.
38. S. Vaziri et al., *IEEE Electron Device Lett.* **41**, 1592–1595 2020).
39. C. Fenouillet-Beranger et al., *IEEE Trans. Electron Dev.* **68**, 3142–3148 (2021).
40. J. Xu et al., *Inorg. Chem.* **35**, 845–849 (1996).
41. S. C. Hunter, F. R. N. Nabarro, R. E. Peierls, *Proc. R. Soc. London. Ser. A.* **220**, 542–561 (1953).
42. K. Tanaka, T. Watanabe, *Jpn. J. Appl. Phys.* **11**, 1429 (1972).
43. T. Peng et al., *Phys. Rev. B* **106**, 125310 (2022).
44. A. Molinari et al., *ACS Appl. Electron. Mater.* **5**, 2624–2637 (2023).
45. H. J. Han et al., *Adv. Mater.* **35**, e2208965 (2023).
46. H. T. Yi, Y. N. Gartstein, V. Podzorov, *Sci. Rep.* **6**, 23650 (2016).
47. C. Wang, T. Cheng, Z. Liu, F. Liu, H. Huang, *Phys. Rev. Lett.* **128**, 056401 (2022).
48. A. Pyzyna et al., in *2017 IEEE International Interconnect Technology Conference (IITC)* (IEEE, 2017), pp. T120–T121; https://doi.org/10.1109/VLSIT.2015.7223712.

SUPPLEMENTARY MATERIALS

science.org/doi/10.1126/science.adq7096
Materials and Methods
Supplementary Text
Figs. S1 to S18
Table S1
References

Science

AAAS

Supplementary Materials for

Surface conduction and reduced electrical resistivity in ultrathin noncrystalline NbP semimetal

Asir Intisar Khan *et al*.

Corresponding authors: Il-Kwon Oh, ikoh@ajou.ac.kr; Eric Pop, epop@stanford.edu

The PDF file includes:

Materials and Methods
Supplementary Text
Figs. S1 to S18
Table S1
References

Materials and Methods

Materials Deposition

In this work, we prepared four types of film samples:

1) **NbP/Nb films** on insulating r-plane sapphire (Al_2O_3) or MgO substrates. These were sputter-deposited at 400 °C (**fig. S1, table S1**), a temperature compatible with back-end-of-the-line semiconductor fabrication. Direct current (dc) magnetron sputtering was performed at 20 W power and 3 mTorr pressure. To reduce lattice mismatch between the substrate and NbP, we first deposited a thin buffer (seed) layer of Nb between 1.4 to 4 nm thickness (*29*). Then, the NbP film was deposited, ranging from 1.5 nm to 80 nm thickness, at a rate of 1.1 nm/min. The Nb seed and NbP deposition were at 400 °C, a temperature which was optimized (in the 300 to 800 °C range) to produce films with lowest resistivity.

2) **NbP/Nb films** on SiO_2 (amorphous) on Si substrates. The NbP thickness was 2.6 nm and 4.3 nm, the Nb seed thickness was 4 nm, and depositions conditions were as stated above.

3) **Cu/Nb films** with 4 nm Nb seed layer, on r-plane sapphire. The Nb seed was deposited as stated above, and Cu metal films (2.5 nm to 20 nm thick) were sputtered at room temperature.

4) **Nb films** on r-plane sapphire with the same thickness as the Nb seed layers used for NbP.

All film samples in this work were capped with 3 to 4 nm thin SiN_x layer, deposited at room temperature, to prevent surface oxidation. All layers were deposited without breaking vacuum.

Materials Characterization

We used a double spherical aberration (Cs) corrected transmission electron microscopy (Themis Z, ThermoFisher Scientific) with an 80 pm resolution and an acceleration voltage of 200 kV. For the atomic-resolution imaging with high angle annular dark field (HAADF) scanning transmission electron microscopy (STEM), we used a probe convergence angle of 15.3 mrad and the inner collection semi angles of 70 mrad and 200 mrad. Energy dispersive spectroscopy (EDS) with four windowless detectors (SuperXG2) was used for the composition mapping of our NbP samples. X-ray photoelectron spectroscopy (Thermo Fisher Scientific, NEXSA) was performed with 400 μm^2 of X-ray spot size and 1000 eV of ion gun energy.

Device Fabrication and Electrical Measurement

After film deposition, the substrates were cut into rectangular shapes (7.5×8.5 mm^2). On these, we patterned standard Hall bar devices (**Fig. 3A**) using direct-write lithography (Heidelberg MLA 150) followed by reactive ion etching of the SiN$_x$/NbP/Nb stack. For the reactive ion etching, we used 30 sccm Cl$_2$ / 10 sccm CH$_4$, 60 W RF power at a pressure of 10 mTorr. Contacts were directly wirebonded (punching through the thin SiN$_x$ capping layer) to the top and side Hall bar edges. All temperature-dependent electrical transport measurements (5 to 300 K) were performed under vacuum in a Quantum Design Dynacool system, using the geometry shown in Fig. 3a. Magnetoresistance measurements used magnetic fields up to $\pm$ 9 T in the out-of-plane direction. Additional room temperature electrical resistivity measurements (Fig. 1d,e) were performed in a Lakeshore 8404 Hall measurement system and an LEI1500 Eddy current system.

Supplementary Text

Section I: Surface and Bulk Conductance of NbP/Nb and NbP Layer

We can write the total sheet conductance, G (in S·□) of our NbP/Nb films at temperature T as:

$$G(t_{Nb}, t_b, T) = G_{Nb}(t_{Nb}, T) + \underbrace{G_b(t_b, T) + G_s(T)}_{G_{NbP}} \tag{1}$$

Where G_{Nb} is the Nb seed layer conductance, G_b is the bulk NbP conductance, G_s is the NbP surface conductance, t_{Nb} and t_b are the Nb seed layer and NbP film thickness, respectively. Here, $G_b = \sigma_b(T)t_b$, is the product of the bulk NbP conductivity and the NbP thickness.

From the total sheet conductance G of NbP/Nb films with varying thicknesses (**Fig. 3C** and **fig. S6D**), we can extract the bulk and surface conductance contributions of the NbP/Nb heterostructure at different temperatures (**fig. S14**) by rearranging eq. (1):

$$G(t_{Nb}, t_b, T) = G_b(t_b, T) + \underbrace{G_{Nb}(t_{Nb}, T) + G_s(T)}_{G_{s,NbP/Nb}} \tag{2}$$

Where, the extracted $G_{s,NbP/Nb}$ is the 'effective' surface conductance which includes the conduction contribution of the bottom NbP surface and the 4 nm Nb seed layer.

Next, we calculated the conductance of the NbP layer (**Fig. 3D**) by subtracting the conductance of the Nb seed layer (measured separately, **fig. S6C**) from the total sheet conductance, G of NbP/Nb films (**Fig. 3C**) using $G_{NbP} = G(t_{Nb}, t_b, T) - G_{Nb}(t_{Nb}, T)$. We then extract the T-dependent resistivity ($\rho_b = t_b/G_{NbP}$) of four different thicknesses of NbP ($t_b \approx 4.3, 9, 18, 80$ nm) (**Fig. 3E**) and subsequently estimated $\sigma_b(T)$ and $G_s(T)$ from $G_{NbP} = \sigma_b(T)t_b + G_s(T)$ (**fig. S12A**, **Fig. 3F, fig. S13A**).

Instead of an ideal two-dimensional surface with thickness $t_s = 0$ Å (as in **fig. S12A**), if we assume that NbP has a finite surface thickness $t_s = 5$ Å (**fig. S12B**), the total conductance of NbP is $G_{NbP} = \sigma_b(T)(t_b - t_{s,}) + \sigma_s(T)t_s$. In this case, the estimated bulk and surface conductance of four different thicknesses of NbP films are shown in **fig. S13B**, between 5 K to 300 K. Here, the bulk conductance increases with temperature from 5 K to 300 K. In contrast, the surface conductance decreases with increasing temperature, and as the NbP is thinned from 80 nm to 4.3 nm, the bulk channel contribution to the conductance decreases for thinner films.

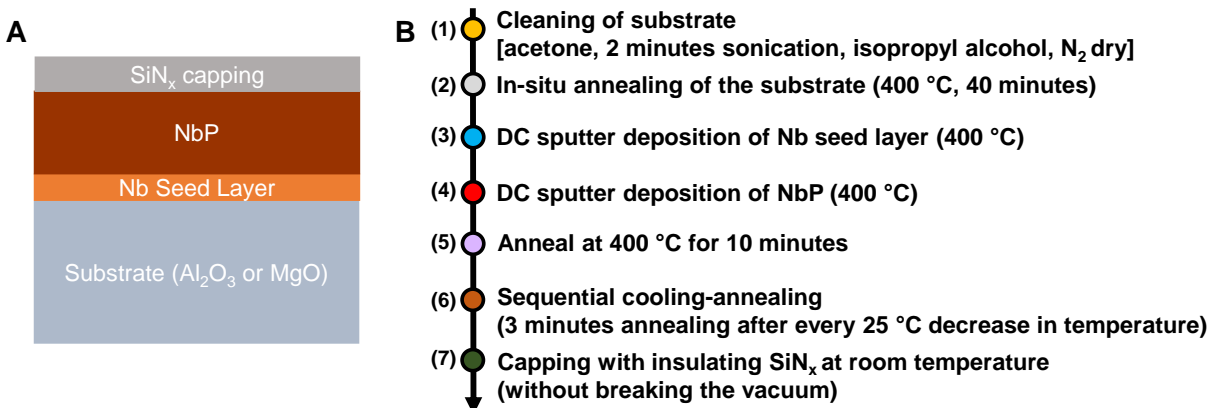## Section II: Carrier Density and Mobility Estimation

We estimate an effective sheet carrier density (in cm^{-2}) $n = 1/(qR_H)$, where q is the elementary charge and R_H is the Hall coefficient (slope of the transverse Hall resistance R_{xy} vs. magnetic field B at 5 K temperature, in **Fig. 4A**) shown in **fig. S17**. From the estimated carrier density n (here, holes) and the sheet conductance of NbP (G_{NbP}) we obtain an effective mobility $\mu = G_{NbP}/(qn)$.

The longitudinal sheet conductance $G_{NbP} = \sigma_b t_b + G_s$ and the transverse (Hall) conductance $G_{xy} = (\sigma_b t_b + G_s)^2/[B(\sigma_b^2 t_b^2 R_{H,b} + G_s^2 R_{H,s})]$, where $R_{H,s}$ and $R_{H,b}$ are Hall coefficients of the surface and bulk charge carriers (holes), respectively. We can rearrange this expression as $R_H = 1/(qn) = 1/(BG_{xy}) = R_{H,b} (\sigma_b t_b)^2(\sigma_b t_b + G_s)^{-2} + R_{H,s} (G_s)^2(\sigma_b t_b + G_s)^{-2}$. When the film thickness approaches zero, we can write $R_H(t_b \rightarrow 0) = R_{H,b} \times 0 + R_{H,s} \times 1 = R_{H,s}$. In other words, as t_b approaches zero, $BG_s = 1/R_{H,s}$. Then, from the measured Hall coefficient R_H vs. NbP thickness, we can estimate $R_{H,s}$ by finding the $t_b \rightarrow 0$ limit of R_H (**fig. S17**). To estimate the uncertainty of this approach, we used the measured R_H of our thinnest NbP film (here 4.3 nm) as a lower bound for $R_{H,s}$.

We can estimate the surface mobility, $\mu_s = G_s/(qn_s)$, where $n_s = 1/(qR_{H,s})$. To extract the carrier density and mobility of NbP, we subtract the Hall conductance of the 4 nm Nb seed layer (**fig. S15A**) from that of the NbP/Nb film stacks (**fig. S15B**), using $G_{xy,NbP} = G_{xy} - G_{xy,Nb}$, where G_{xy} is the measured total Hall conductance of the NbP/4 nm Nb film, and $G_{xy,Nb}$ is the Hall conductance

of our reference 4 nm Nb seed film. We note that the Hall measurement of our 4 nm Nb film (**fig. S15A**) yields 2.17×10^{23} cm^{-3} volumetric carrier density, ~2× higher than the carrier density reported in Ref. (*49*). The Nb seed layer also shows superconducting behavior below 2.5 K (**Fig. S6B**), as expected in such thin films (*49, 50*).

We repeated our transport analysis of Fig. 4 in the main text *without* subtracting the contribution of 4 nm Nb seed, as shown in **fig. S18**. Here, we find that even for the NbP/Nb heterostructures, the transport *trends* described in Fig. 4 from the main text (e.g., carrier density, mobility) remain unchanged. NbP/Nb heterostructures (including 4 nm Nb seed) also show a decreasing carrier density, and an increasing mobility with decreasing total stack thickness.

A

SiN$_x$ capping

NbP

Nb Seed Layer

Substrate (Al$_2$O$_3$ or MgO)

B

(1) Cleaning of substrate
[acetone, 2 minutes sonication, isopropyl alcohol, N$_2$ dry]

(2) In-situ annealing of the substrate (400 °C, 40 minutes)

(3) DC sputter deposition of Nb seed layer (400 °C)

(4) DC sputter deposition of NbP (400 °C)

(5) Anneal at 400 °C for 10 minutes

(6) Sequential cooling-annealing
(3 minutes annealing after every 25 °C decrease in temperature)

(7) Capping with insulating SiN$_x$ at room temperature
(without breaking the vacuum)

Fig. S1. Materials deposition steps. (A) Schematic of the NbP semimetal stack on top of a thin Nb seed layer. **(B)** Sputtering steps which form the NbP thin film stacks. The chamber base pressure was kept below 5×10^{-8} Torr. See **Materials and Methods: Materials Deposition** section for additional details.
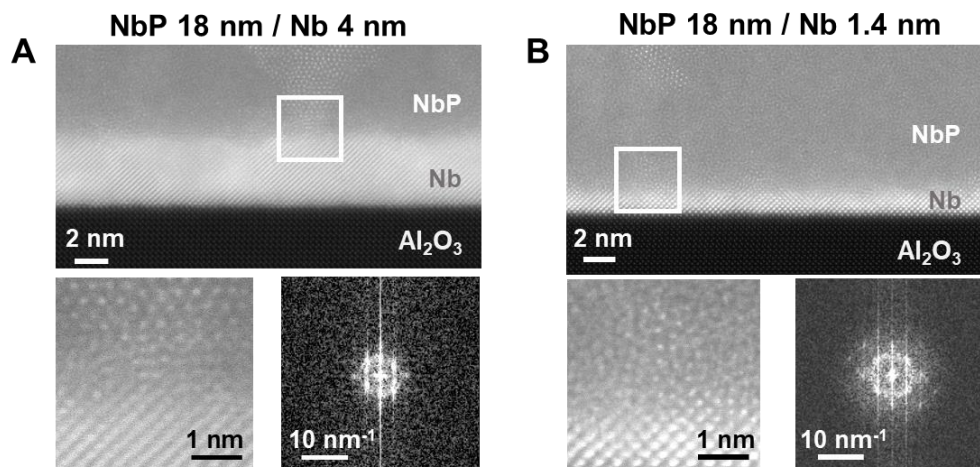
Fig. S2. STEM and diffraction patterns of NbP films. High resolution HAADF-STEM and zoomed-in images and corresponding diffraction patterns for **(A)** 18 nm NbP film on a 4 nm Nb, and **(B)** 18 nm NbP on a 1.4 nm Nb seed layer, showing a similar nano-crystallinity of the NbP films near the NbP/Nb interface for both 4 nm and 1.4 nm Nb seed layers. We note that the Nb seed layer shows a comparable crystalline quality as the control films (**fig. S3**), and its resistivity is much higher in the thinnest films (see Fig. 1D) compared to that of the NbP/Nb stack.
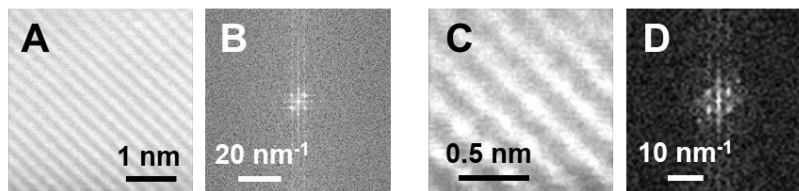
Fig. S3. STEM and diffraction patterns of control thin Nb films. High-resolution HAADF-STEM and diffraction patterns of **(A,B)** a 4 nm Nb, and **(C,D)** a 1.4 nm Nb film showing a similar degree of crystallinity compared to the Nb seed layers in the NbP/Nb stack.
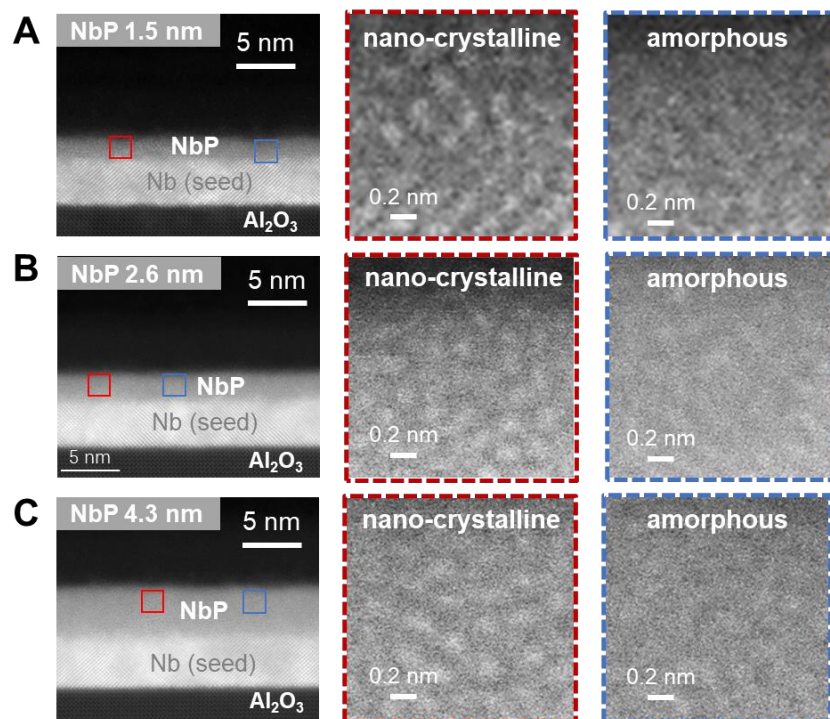
**Fig. S4**. **STEM characterization of NbP films on 4 nm Nb seed**. Zoomed-in HAADF-STEM images of **(A)** 1.5 nm, **(B)** 2.6 nm, and **(C)** 4.3 nm NbP films on a 4 nm Nb seed layer showing the presence of local short-range ordering and nano-crystallinity (red-box panels) within the amorphous NbP film matrices. Red and blue box panels display representative nano-crystalline and amorphous regions, respectively.
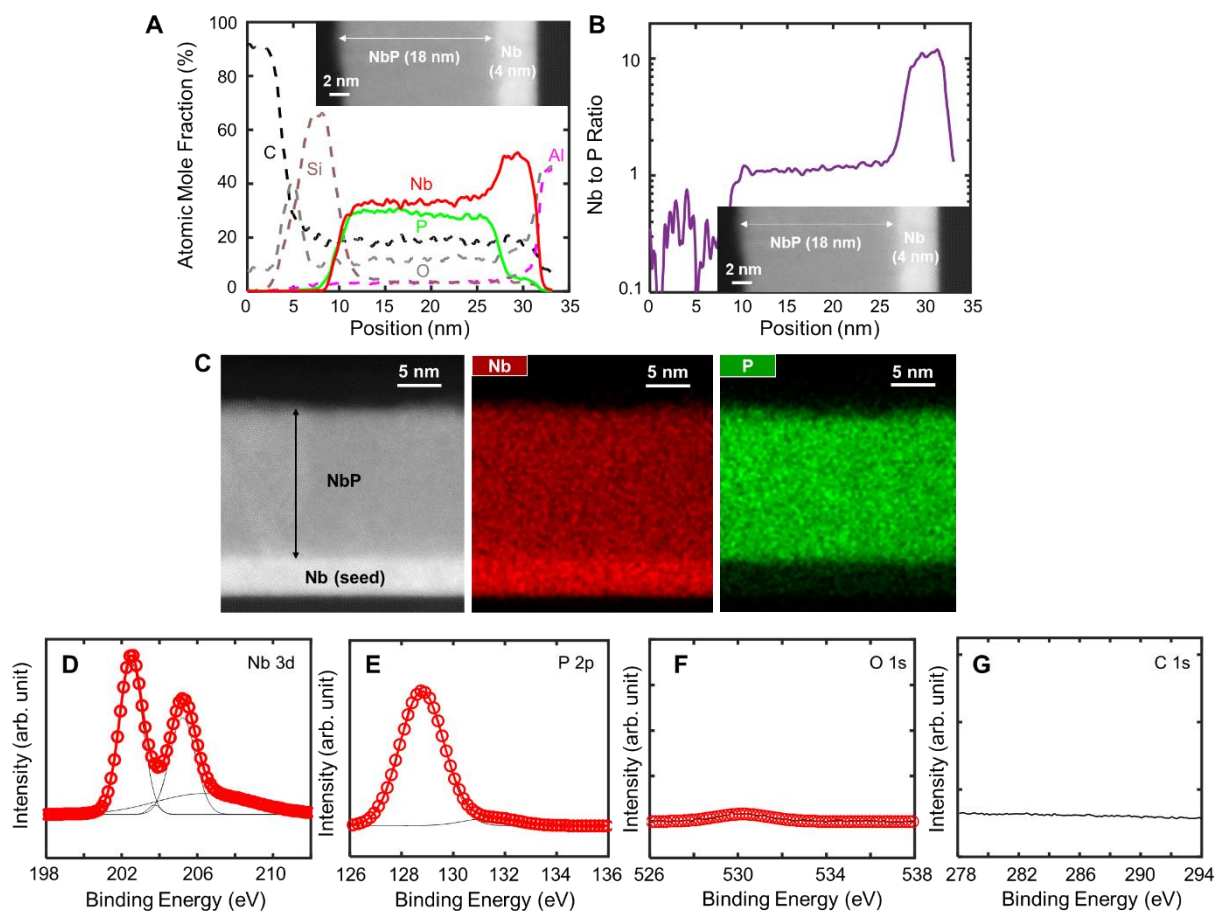
Fig. S5. EDS and XPS characterization of NbP/Nb film. (A,B) Energy dispersive spectra (EDS) line scans showing the atomic ratio between Nb and P in our NbP film (here ~18 nm) to be close to 1. **(C)** EDS compositional mapping performed from HAADF-STEM confirming the homogeneity of Nb and P across the NbP sample. The presence of C and O elements in EDS characterization could be due to hydrocarbons adsorbed onto the sample surface, and surface oxidation during sample preparation. XPS spectra of an 18 nm NbP/4 nm Nb film (after 120 s etching): **(D)** Nb 3d, **(E)** P 2p, **(F)** O 1s, and **(G)** C 1s core levels, display no significant carbon incorporation and a small percentage (~4 %) of O inside the NbP layer.
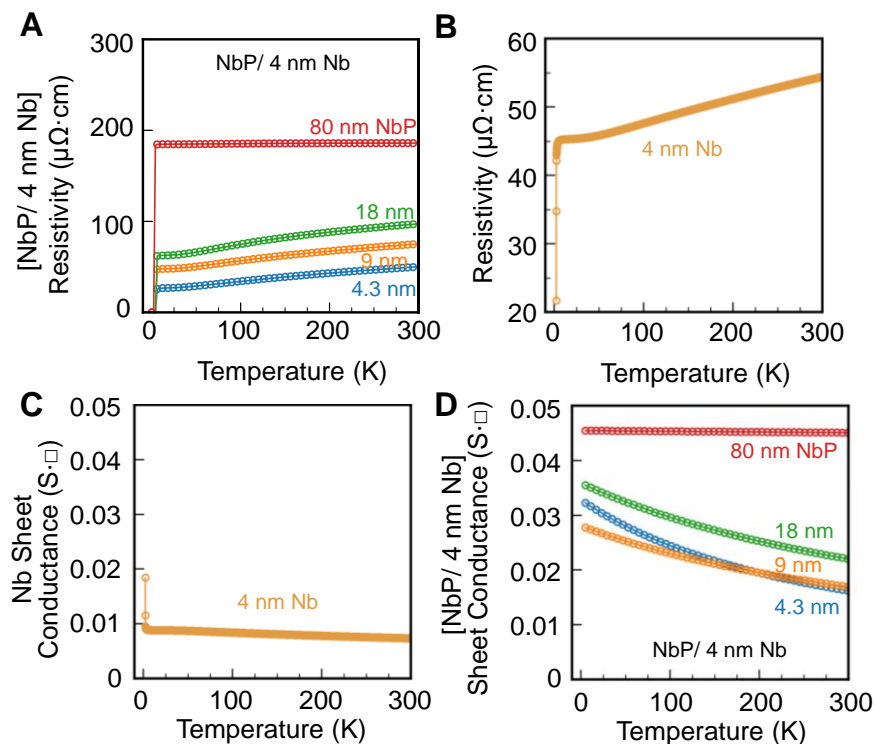
**Fig. S6. Temperature-dependent electrical measurement of Nb and NbP/Nb heterostructure**. Temperature dependent resistivity of **(A)** NbP/Nb films with varying NbP thickness (here 4.3, 9, 18, and 80 nm) on a 4 nm Nb seed, and **(B)** control 4 nm Nb film. Temperature-dependent sheet conductance of **(C)** control 4 nm Nb and **(D)** NbP/Nb films with varying NbP thickness (here 4.3, 9, 18, and 80 nm) on a 4 nm Nb seed. (Note, this is the same figure as Fig. 3C in the main manuscript, repeated here for convenience.) We note the resistivity in **A** is the total resistivity for the entire thickness of the sample (i.e., 8.3 nm to 84 nm), including the contribution of the 4 nm Nb seed layer. The control 4 nm Nb sample in **B,C** was prepared with the same deposition conditions as the 4 nm Nb seed layer under the NbP samples in **A,D**. The Nb seed layer is on the same sapphire substrate, capped by SiN_x (see Materials and Methods, page 2 of this document).
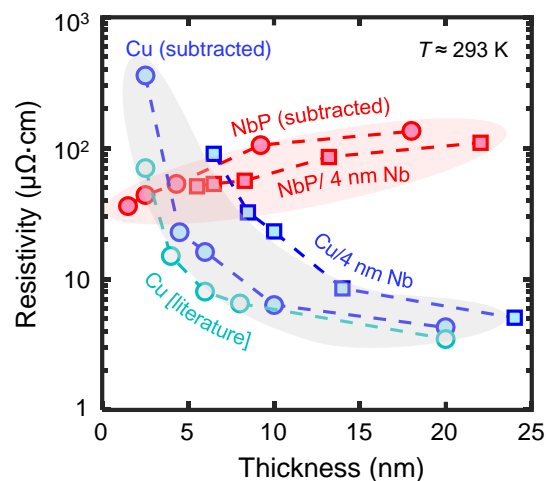
Fig. S7. Electrical Resistivity of Cu/Nb and NbP/Nb stacks. Room temperature resistivity vs. thickness of Cu/(4 nm Nb) heterostructures before (squares) and after (circles) subtracting the Nb seed layer conduction contribution. Unlike NbP/(4 nm Nb) heterostructures and NbP layers (after subtraction), the resistivity *increases* with decreasing total thickness for both Cu/(4 nm Nb) heterostructures and the Cu layers (using identical subtraction scheme). The resistivity of the Cu layer (after subtraction) as well as the resistivity vs. thickness trend are in agreement with the reported literature (*48*). We also note that in the Cu/Nb heterostructures, the bulk-like value nearly recovers the bulk resistivity of Cu (few $\mu\Omega\cdot$cm). Both types of films are capped *in situ* with the same SiN_x layer (~3 nm) as described in Materials and Methods.
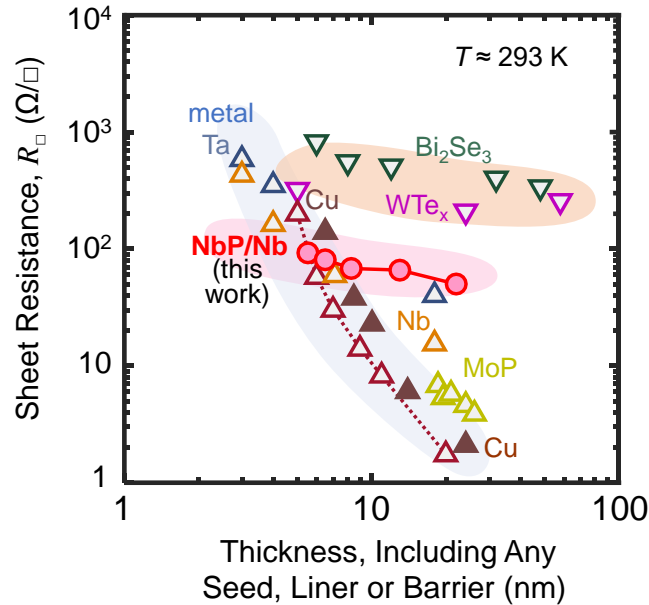
Fig. S8. Room temperature ($T \approx 293$ K) sheet resistance $R_\square$ vs. total thickness for various materials including our sputtered NbP semimetal (with 4 nm Nb seed), conventional metals like Cu (with liner and barrier, hollow triangles) (*48*), control Cu with Nb seed (from this work, filled triangles), Ta, Nb (from this work), other topological insulators (e.g., Bi_2Se_3) (*32*), topological semimetals (nanocrystalline WTe_x) (*23, 26*), and a topological metal (MoP) (*45*) from the literature. Here, sheet resistance $R_\square = R_{meas}(W/L)$, where R_{meas} is the measured resistance, L and W are the length and width of the samples, respectively. The sheet resistance of topological semimetals (NbP, WTe_x) and topological insulators (Bi_2Se_3) display a slowly increasing trend with decreasing thickness (shaded red and orange). In contrast, the sheet resistance of conventional metals increases much more strongly with decreasing thickness (shaded light blue trend), a bottleneck for future nanoelectronics. For a thickness decrease from ~20 nm down to ~5 nm, the sheet resistance of traditional metals increases by ~10× to 100×, whereas the sheet resistance of topological semimetals (and insulators) increases by only < 2×, demonstrating the unique potential of such materials in achieving low resistivity even at their ultra-scaled thicknesses.
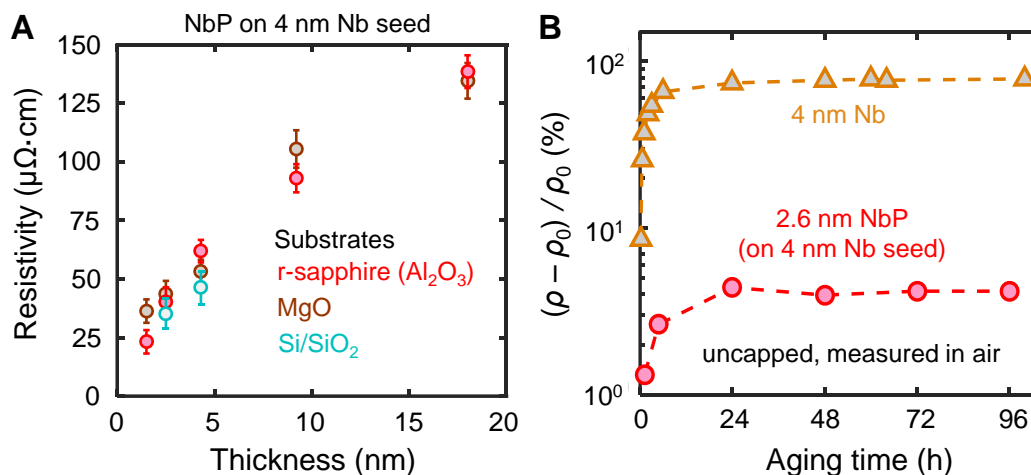
Fig. S9. Electrical resistivity measurement of NbP. (**A**) Resistivity versus thickness of NbP films on Al$_2$O$_3$ (sapphire), MgO and SiO$_2$/Si substrates. (**B**) Percentage change in the resistivity versus aging time for a ~2.6 nm thin NbP and a control 4 nm Nb metal films measured in air. ρ_0 is the resistivity measured immediately after deposition of the films, and ρ is the resistivity measured after aging time steps. All the measurements (**A,B**) are taken at room temperature. NbP thin films were sputtered on 4 nm Nb seed layer. We subtracted the thickness and conductance contribution of the 4 nm Nb seed layer from the NbP/Nb stack.
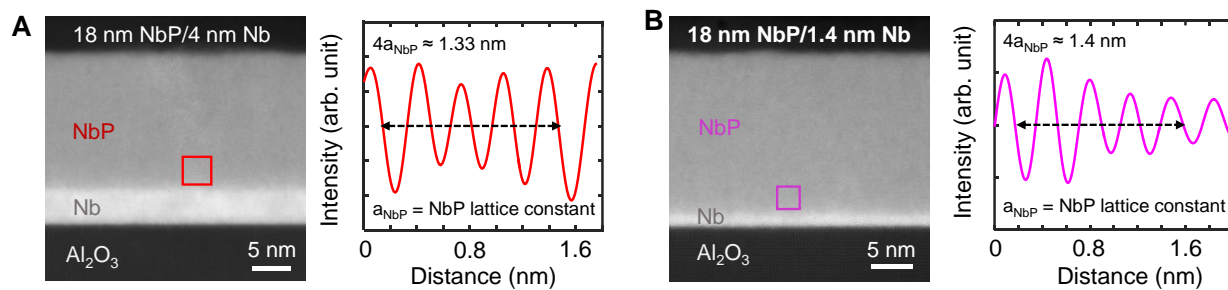
Fig. S10. Microstructure details of NbP/Nb heterostructures. Local nanocrystalline (short-range order) region of ~18 nm thin NbP film on **(A)** 4 nm Nb seed, showing NbP lattice constant ~3.33 Å, close to it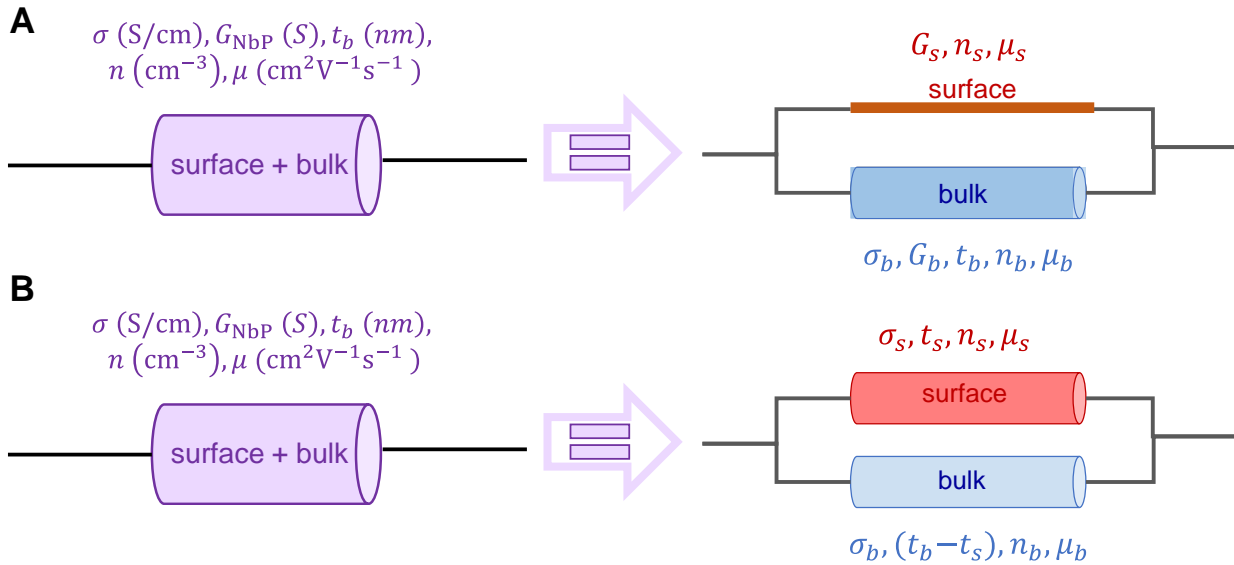s nominal value of ~3.332 Å. **(B)** Similar image on 1.4 nm Nb seed layer, revealing NbP lattice constant ~3.5 Å, which indicates ~18 nm NbP is strained on the thinner Nb seed.
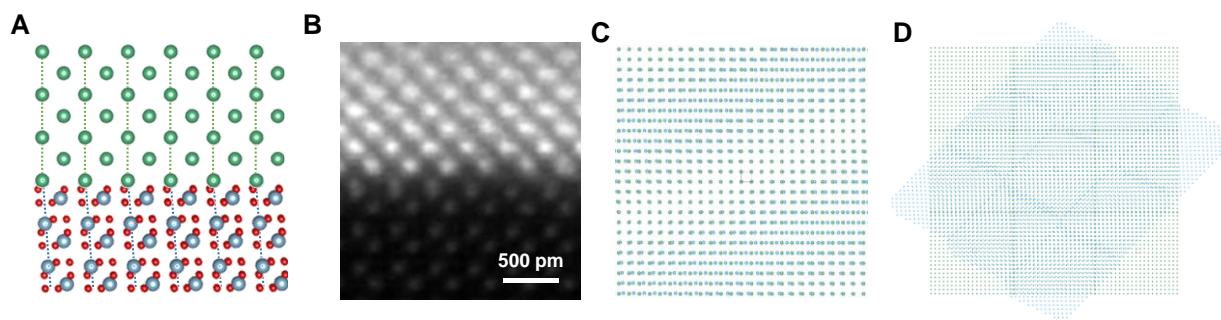
Fig. S11. Strain and lattice constant of NbP on different Nb seed layers. (A) Atomic projection of Nb [010] and Al_2O_3 [$\bar{2}$11]. **(B)** Atomic-resolution HAADF-STEM image of **A**. **(C)** Atomic projection of the Nb atoms in Nb (100) on Al atoms in Al_2O_3 (102). We assume that the distance of Nb-Nb (original distance = 3.32 Å) is the same as that of Al-Al (3.53 Å). **(D)** Wide projection view of (C) which shows the Moiré fringe. Nb in Nb (100) plane has a square lattice, while Al in α-Al_2O_3 (102) has a rhombus lattice tilted by 6° compared to the square, which is clearly shown in the diffraction pattern using Fourier transform in Fig. 2E. Even if the atomic distance is the same, the coherency is periodically broken and misfit strain occurs in-plane, which is observed by Moiré pattern in projection of Nb (100) plane and α-Al_2O_3 (102) plane in fig. S8D. Thus, the interface between Nb (100) and α-Al_2O_3 (102) is semi-coherent interface and misfit dislocation should be introduced to release the strain energy as the thickness of Nb increases. The misfit dislocation is introduced at every 6 nm on the calculation by lattice mismatch and the Moiré distance due to lattice distortion is 3 nm. In our case, misfit dislocation was found at ~4 nm distance. Consequently, after the insertion of dislocation at ~1.5 nm thickness of Nb layer, the Nb lattice releases the compressive stress and returns to the original cubic structure with $a = 3.32$ Å. In the case of the 1.4 nm Nb sample, misfit dislocation releasing the stress could not be observed within the Nb film, which means that the compressive stress due to lattice tensile ($a = 3.53$ Å) remains in 1.4 nm Nb film.

A

σ (S/cm), G_{NbP} (S), t_b (nm), n (cm^{-3}), μ (cm^{2}V^{-1}s^{-1})

surface + bulk

G_s, n_s, μ_s

surface

bulk

$\sigma_b, G_b, t_b, n_b, \mu_b$

B

σ (S/cm), G_{NbP} (S), t_b (nm), n (cm^{-3}), μ (cm^{2}V^{-1}s^{-1})

surface + bulk

$\sigma_s, t_s, n_s, \mu_s$

surface

bulk

$\sigma_b, (t_b - t_s), n_b, \mu_b$

Fig. S12. **Surface- and bulk-channel conduction estimation for NbP**. The total sheet conductance, G_{NbP} of our NbP sample with a thickness t_b can be modeled as $G_{\text{NbP}} = G_b(t_b,T) + G_s(T)$, (**A**) Considering zero surface thickness, i.e., ideal two-dimensional (2D) surface with a sheet conductance G_s. (**B**) Considering a finite surface thickness $t_s = 5$ Å with $G_{\text{NbP}} = \sigma_b(T)(t_b - t_s) + G_s(T)$, where $G_s = \sigma_s t_s$. The 2D surface carrier density is n_s, the surface carrier mobility is μ_s, G_b is the bulk NbP conductance, G_s is the NbP surface conductance, and T is the temperature. The bulk conductivity is σ_b (the inverse of resistivity, $1/\rho_b$) and the surface conductivity is σ_s.
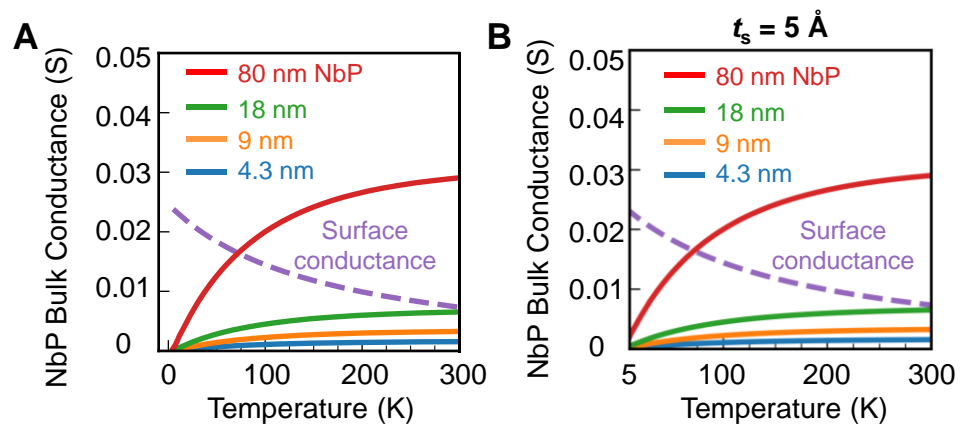
Fig. S13. **Bulk and surface conductance fits for NbP**. NbP bulk conductance and surface conductance for varying thicknesses of NbP films vs. temperature considering **(A)** an ideal 2D surface with zero surface thickness, and **(B)** a finite surface thickness $t_s = 5$ Å for NbP.
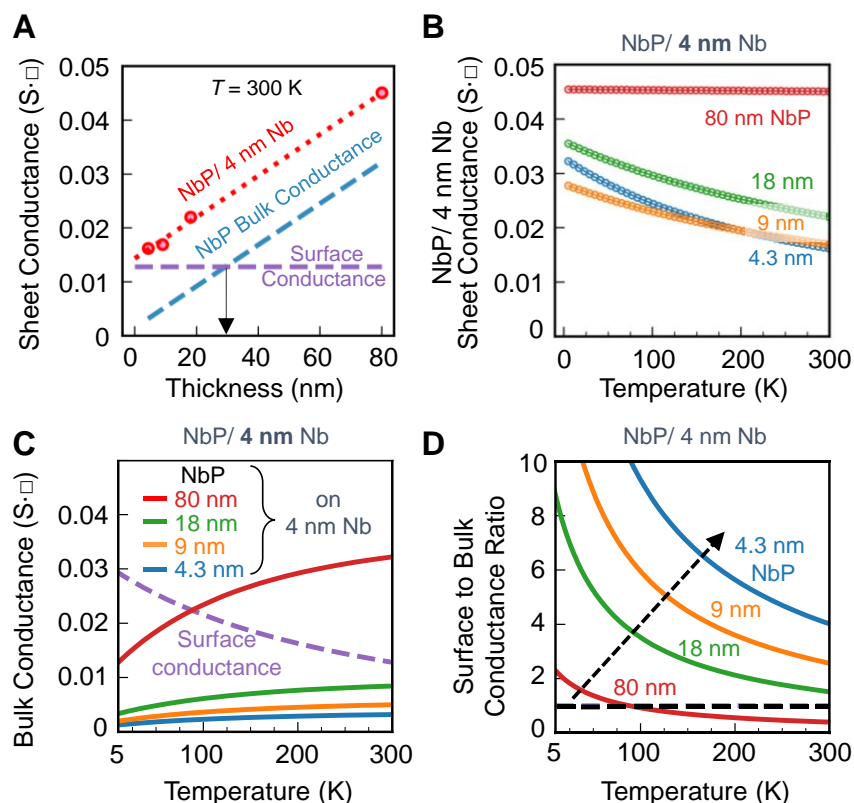
Fig. S14. **Temperature-dependent transport of NbP/Nb heterostructure**. **(A)** Room temperature sheet conductance of NbP/ 4 nm Nb heterostructures vs. NbP thickness. Red dotted line is a fit to the total sheet conductance of the NbP/ Nb heterostructures. NbP bulk conductance and 'effective surface conductance' (NbP surface conductance and 4 nm Nb seed conductance) are obtained through this fit (Materials and Methods section: Surface and Bulk Conductance of NbP/Nb and NbP Layer). The black arrow shows that the surface conductance dominates the total sheet conductance at room temperature for NbP/Nb films thinner than ~30 nm. **(B)** Temperature dependent sheet conductance of NbP / 4 nm Nb samples with varying NbP thicknesses (here 4.3, 9, 18, and 80 nm) on a 4 nm Nb seed. **(C)** Two-channel conductance fit (Materials and Methods: Surface and Bulk Conductance of NbP/Nb and NbP Layer) to the data in fig. S14B for various film thicknesses, indicating a metallic surface-channel (dashed line) and disorder dominated bulk channel conductance (solid lines). **(D)** Surface to bulk conductance ratio versus temperature for our NbP/Nb samples, showing that with decreasing film thicknesses, surface to bulk conductance ratio increases (indicated by the arrow). The region above the dashed line represents the surface conductance dominated area.
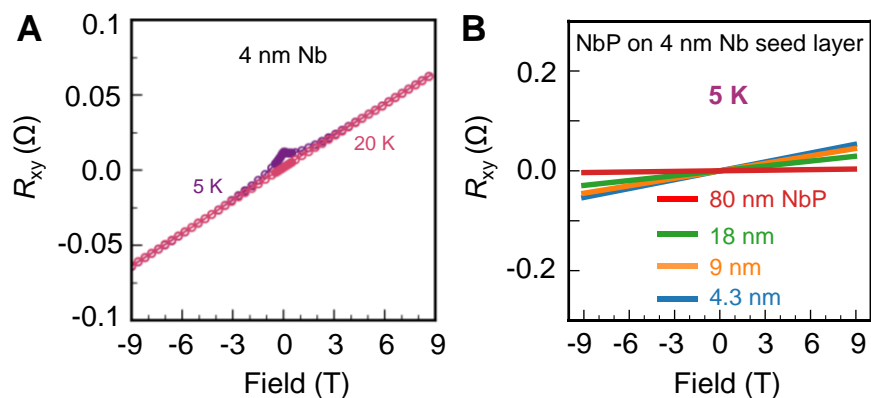
Fig. S15. Magnetic field dependent Hall resistance measurements for Nb and NbP/Nb. Hall resistance versus magnetic field of **(A)** control 4 nm Nb at 5 K and 20 K temperatures and **(B)** NbP/ 4 nm Nb samples for varying NbP thicknesses (80, 18, 9 and 4.3 nm) on a 4 nm Nb seed (at 5 K temperature). The control 4 nm Nb sample in **A** was prepared with the same deposition conditions as for the 4 nm Nb seed layer beneath the NbP samples in **B**.
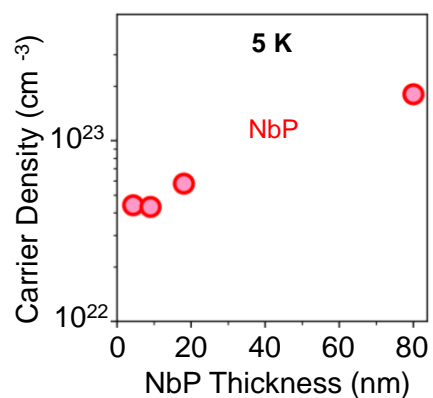
Fig. S16. Total effective carrier density for NbP. Estimated total carrier density (holes, per unit volume) (extracted from Fig. 4A) for various NbP film thicknesses. The corresponding sheet carrier density (in cm^{-2}) is shown in Fig. 4C. We note that total effective carrier density from Hall measurements in non-crystalline or disordered systems (as our non-crystalline NbP) could be overestimated (and the mobility underestimated) due to possible contribution from hopping-like transport (*46*). A similar observation has been reported in other systems such as organic semiconductors (*46*) and the topological insulator Bi_2Se_3, where the total carrier density in non-crystalline Bi_2Se_3 was estimated ~10× larger (*25*) compared to its crystalline counterpart (*32*).
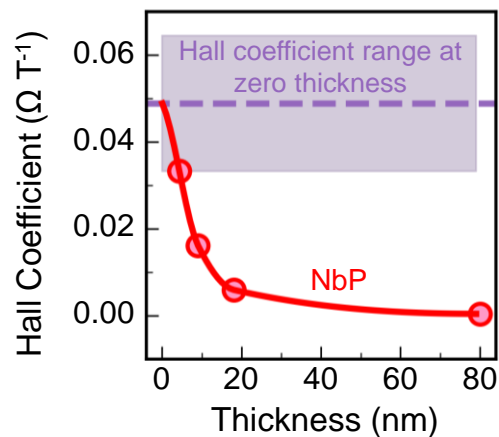
Fig. S17. Hall coefficient measurements for NbP. Measured Hall coefficient versus thickness of NbP films. Red line is a fit to the data extracted from measurements. Based on this fit, the purple dotted line represents the Hall coefficient when the NbP sample thickness → 0. As a conservative estimate for such a scenario, the Hall coefficient of the thinnest NbP sample (here, 4.3 nm) is defined as a lower bound (the bottom of the shaded purple region) for the Hall coefficient.
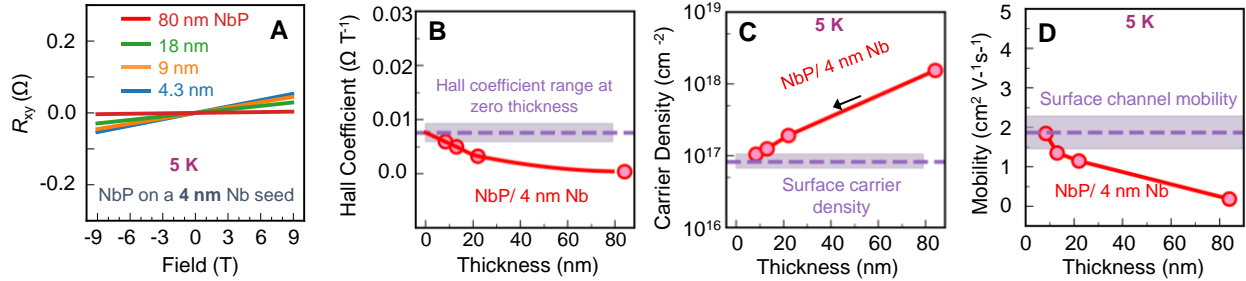
Fig. S18. **Magnetic field dependent transport of NbP/ 4 nm Nb stacks**. **(A)** Hall resistance versus magnetic field for NbP/ 4 nm Nb films at 5 K temperature. **(B)** Measured Hall coefficient versus thickness of NbP/ 4 nm Nb film stacks. Red line is a fit to the data extracted from measurements. Based on this fit, the purple dotted line represents the Hall coefficient when the NbP/4 nm Nb stack total thickness tends to 0 (similar approach as in **fig. S17**). **(C)** Two-dimensional (sheet) carrier density (extracted from fig. S17A,B) showing a decrease in the carrier density with decreasing NbP/4 nm Nb total film thicknesses. The shaded purple region represents the sheet carrier density in the limit of zero NbP/ 4 nm Nb total film thickness. **(D)** Mobility of the NbP/ 4 nm Nb samples, showing an increasing trend with decreasing total sample thicknesses. The shaded region represents the range of the surface channel mobility, estimated from the surface carrier density. As the films get thinner, the total mobility approaches the surface channel mobility. Thus, the inclusion of the 4 nm Nb seed layer conductivity contribution to the NbP films does not alter the trends discerned in Fig. 4. We note that carrier density estimated from Hall measurements in non-crystalline or disordered systems could be overestimated (and the mobility underestimated) due to possible contribution from hopping-like transport (*46*).

Material	Power (W)	Pressure (mTorr)	Gas flow (sccm)	Temperature
Nb (seed layer)	30 (DC)	3	Ar: 20	400 ℃
NbP	15 (DC)	3	Ar: 20	400 ℃
SiN$_x$ (capping layer)	100 (RF)	4	Ar: 30	Room temperature

Table S1. Materials deposition parameters. Sputtering parameters for various materials used in this work. DC: direct current, RF: radio frequency.

References and Notes

1. S. Salahuddin, K. Ni, S. Datta, The era of hyper-scaling in electronics. *Nat. Electron.* **1**, 442–450 (2018). doi:10.1038/s41928-018-0117-x

2. A. A. Vyas, C. Zhou, C. Y. Yang, On-chip interconnect conductor materials for end-of-roadmap technology nodes. *IEEE Trans. Nanotechnol.* **17**, 4–10 (2018). doi:10.1109/TNANO.2016.2635583

3. M. M. Shulaker, G. Hills, R. S. Park, R. T. Howe, K. Saraswat, H. P. Wong, S. Mitra, Three-dimensional integration of nanotechnologies for computing and data storage on a single chip. *Nature* **547**, 74–78 (2017). doi:10.1038/nature22994 Medline

4. D. Ielmini, H.-S. P. Wong, In-memory computing with resistive switching devices. *Nat. Electron.* **1**, 333–343 (2018). doi:10.1038/s41928-018-0092-2

5. S. Jung, H. Lee, S. Myung, H. Kim, S. K. Yoon, S.-W. Kwon, Y. Ju, M. Kim, W. Yi, S. Han, B. Kwon, B. Seo, K. Lee, G.-H. Koh, K. Lee, Y. Song, C. Choi, D. Ham, S. J. Kim, A crossbar array of magnetoresistive memory devices for in-memory computing. *Nature* **601**, 211–216 (2022). doi:10.1038/s41586-021-04196-6 Medline

6. L. Zhu, K. Sobotkiewich, X. Ma, X. Li, D. C. Ralph, R. A. Buhrman, Strong damping-like spin-orbit torque and tunable Dzyaloshinskii–Moriya interaction generated by low-resistivity $Pd_{1-x}Pt_x$ alloys. *Adv. Funct. Mater.* **29**, 1805822 (2019). doi:10.1002/adfm.201805822

7. V. Huang, D. Shim, H. Simka, A. Naeemi, "From interconnect materials and processes to chip level performance: Modeling and design for conventional and exploratory concepts" in *2020 IEEE International Electron Devices Meeting (IEDM)* (IEEE, 2020), pp. 32.6.1–32.6.4; https://doi.org/10.1109/IEDM13553.2020.9371945.

8. D. Gall, The search for the most conductive metal for narrow interconnect lines. *J. Appl. Phys.* **127**, 050901 (2020). doi:10.1063/1.5133671

9. E. V. Barnat, D. Nagakura, P.-I. Wang, T.-M. Lu, Real time resistivity measurements during sputter deposition of ultrathin copper films. *J. Appl. Phys.* **91**, 1667–1672 (2002). doi:10.1063/1.1430530

10. E. C. Ko, J. Y. Kim, H. Rhee, K. M. Kim, J. H. Han, Low-resistivity ruthenium metal thin films grown via atomic layer deposition using dicarbonyl-bis(5-methyl-2,4-hexanediketonato)ruthenium(II) and oxygen. *Mater. Sci. Semicond. Process.* **156**, 107258 (2023). doi:10.1016/j.mssp.2022.107258

11. D. Gall, "The resistivity bottleneck: The search for new interconnect metals" in *2020 International Symposium on VLSI Technology, Systems and Applications (VLSI-TSA)* (IEEE, 2020), pp. 112–113; https://doi.org/10.1109/VLSI-TSA48913.2020.9203700.

12. C.-T. Chen, U. Bajpai, N. A. Lanzillo, C.-H. Hsu, H. Lin, G. Liang, "Topological semimetals for scaled back-end-of-line interconnect beyond Cu" in *2020 IEEE International Electron Devices Meeting (IEDM)* (IEEE, 2020), pp. 32.4.1–32.4.4; https://doi.org/10.1109/IEDM13553.2020.9371996.

13. N. P. Armitage, E. J. Mele, A. Vishwanath, Weyl and Dirac semimetals in three-dimensional

solids. *Rev. Mod. Phys.* **90**, 015001 (2018). doi:10.1103/RevModPhys.90.015001

14. C. Shekhar, A. K. Nayak, Y. Sun, M. Schmidt, M. Nicklas, I. Leermakers, U. Zeitler, Y. Skourski, J. Wosnitza, Z. Liu, Y. Chen, W. Schnelle, H. Borrmann, Y. Grin, C. Felser, B. Yan, Extremely large magnetoresistance and ultrahigh mobility in the topological Weyl semimetal candidate NbP. *Nat. Phys.* **11**, 645–649 (2015). doi:10.1038/nphys3372

15. S.-Y. Xu, N. Alidoust, I. Belopolski, Z. Yuan, G. Bian, T.-R. Chang, H. Zheng, V. N. Strocov, D. S. Sanchez, G. Chang, C. Zhang, D. Mou, Y. Wu, L. Huang, C.-C. Lee, S.-M. Huang, B. Wang, A. Bansil, H.-T. Jeng, T. Neupert, A. Kaminski, H. Lin, S. Jia, M. Zahid Hasan, Discovery of a Weyl fermion state with Fermi arcs in niobium arsenide. *Nat. Phys.* **11**, 748–754 (2015). doi:10.1038/nphys3437

16. L. Rocchino, F. Balduini, H. Schmid, A. Molinari, M. Luisier, V. Süß, C. Felser, B. Gotsmann, C. B. Zota, Magnetoresistive-coupled transistor using the Weyl semimetal NbP. *Nat. Commun.* **15**, 710 (2024). [doi:10.1038/s41467-024-44961-5](doi:10.1038/s41467-024-44961-5) Medline

17. S.-Y. Xu, I. Belopolski, N. Alidoust, M. Neupane, G. Bian, C. Zhang, R. Sankar, G. Chang, Z. Yuan, C.-C. Lee, S.-M. Huang, H. Zheng, J. Ma, D. S. Sanchez, B. Wang, A. Bansil, F. Chou, P. P. Shibayev, H. Lin, S. Jia, M. Z. Hasan, TOPOLOGICAL MATTER. Discovery of a Weyl fermion semimetal and topological Fermi arcs. *Science* **349**, 613–617 (2015). doi:10.1126/science.aaa9297 Medline

18. J. N. Nelson, A. D. Rice, R. Kurleto, A. Shackelford, Z. Sierzega, P. Hao, B. S. Berggren, C.-S. Jiang, A. G. Norman, M. E. Holtz, J. S. Mangum, I. A. Leahy, K. N. Heinselman, H. Ness, M. Van Schilfgaarde, D. S. Dessau, K. Alberi, Thin-film TaAs: Developing a platform for Weyl semimetal devices. *Matter* **6**, 2886–2899 (2023). doi:10.1016/j.matt.2023.06.018

19. G. Resta, S.-T. Pi, X. Wan, S. Y. Savrasov, High surface conductivity of Fermi-arc electrons in Weyl semimetals. *Phys. Rev. B* **97**, 085142 (2018). doi:10.1103/PhysRevB.97.085142

20. S.-W. Lien, I. Garate, U. Bajpai, C.-Y. Huang, C.-H. Hsu, Y.-H. Tu, N. A. Lanzillo, A. Bansil, T.-R. Chang, G. Liang, H. Lin, C.-T. Chen, Unconventional resistivity scaling in topological semimetal CoSi. *NPJ Quantum Mater.* **8**, 3 (2023). [doi:10.1038/s41535-022-00535-6](doi:10.1038/s41535-022-00535-6)

21. N. B. M. Schröter, D. Pei, M. G. Vergniory, Y. Sun, K. Manna, F. de Juan, J. A. Krieger, V. Süss, M. Schmidt, P. Dudin, B. Bradlyn, T. K. Kim, T. Schmitt, C. Cacho, C. Felser, V. N. Strocov, Y. Chen, Chiral topological semimetal with multifold band crossings and long Fermi arcs. *Nat. Phys.* **15**, 759–765 (2019). [doi:10.1038/s41567-019-0511-y](doi:10.1038/s41567-019-0511-y)

22. M. Breitkreiz, P. W. Brouwer, Large contribution of Fermi arcs to the conductivity of topological metals. *Phys. Rev. Lett.* **123**, 066804 (2019). doi:10.1103/PhysRevLett.123.066804 Medline

23. C. Zhang, Z. Ni, J. Zhang, X. Yuan, Y. Liu, Y. Zou, Z. Liao, Y. Du, A. Narayan, H. Zhang, T. Gu, X. Zhu, L. Pi, S. Sanvito, X. Han, J. Zou, Y. Shi, X. Wan, S. Y. Savrasov, F. Xiu, Ultrahigh conductivity in Weyl semimetal NbAs nanobelts. *Nat. Mater.* **18**, 482–488 (2019). [doi:10.1038/s41563-019-0320-9](doi:10.1038/s41563-019-0320-9) Medline

24. T. Zhou, D. Gall, Resistivity scaling due to electron surface scattering in thin metal layers. *Phys. Rev. B* **97**, 165406 (2018). doi:10.1103/PhysRevB.97.165406

25. P. Corbae, S. Ciocys, D. Varjas, E. Kennedy, S. Zeltmann, M. Molina-Ruiz, S. M. Griffin, C. Jozwiak, Z. Chen, L.-W. Wang, A. M. Minor, M. Scott, A. G. Grushin, A. Lanzara, F. Hellman, Observation of spin-momentum locked surface states in amorphous Bi_2Se_3. *Nat. Mater.* **22**, 200–206 (2023). [doi:10.1038/s41563-022-01458-0](doi:10.1038/s41563-022-01458-0) Medline Mahendra DC,

26. X. Li, P. Li, V. D.-H. Hou, C.-H. Nien, F. Xue, D. Yi, C. Bi, C.-M. Lee, S.-J. Lin, W. Tsai, Y. Suzuki, S. X. Wang, Large and robust charge-to-spin conversion in sputtered conductive WTex with disorder. *Matter* **4**, 1639–1653 (2021). doi:10.1016/j.matt.2021.02.016

27. M. J. Mleczko, R. L. Xu, K. Okabe, H.-H. Kuo, I. R. Fisher, H.-S. P. Wong, Y. Nishi, E. Pop, High current density and low thermal conductivity of atomically thin semimetallic WTe_2. *ACS Nano* **10**, 7507–7514 (2016). doi:10.1021/acsnano.6b02368 Medline

28. J. Schmitz, Low temperature thin films for next-generation microelectronics. *Surf. Coat. Tech.* **343**, 83–88 (2018). doi:10.1016/j.surfcoat.2017.11.013

29. A. Bedoya-Pinto, A. K. Pandeya, D. Liu, H. Deniz, K. Chang, H. Tan, H. Han, J. Jena, I. Kostanovskiy, S. S. P. Parkin, Realization of epitaxial NbP and TaP Weyl semimetal thin films. *ACS Nano* **14**, 4405–4413 (2020). doi:10.1021/acsnano.9b09997 Medline

30. J. Krupka, D. Nguyen, J. Mazierska, Microwave and RF methods of contactless mapping of the sheet resistance and the complex permittivity of conductive materials and semiconductors. *Meas. Sci. Technol.* **22**, 085703 (2011). [doi:10.1088/0957-0233/22/8/085703](doi:10.1088/0957-0233/22/8/085703)

31. L. He, F. Xiu, X. Yu, M. Teague, W. Jiang, Y. Fan, X. Kou, M. Lang, Y. Wang, G. Huang, N.-C. Yeh, K. L. Wang, Surface-dominated conduction in a 6 nm thick Bi_2Se_3 thin film. *Nano Lett.* **12**, 1486–1490 (2012). [doi:10.1021/nl204234j](doi:10.1021/nl204234j) Medline

32. N. Bansal, Y. S. Kim, M. Brahlek, E. Edrey, S. Oh, Thickness-independent transport channels in topological insulator $Bi_{(2)}Se_{(3)}$ thin films. *Phys. Rev. Lett.* **109**, 116804 (2012). doi:10.1103/PhysRevLett.109.116804 Medline

33. N. L. Nair, M.-E. Boulanger, F. Laliberté, S. Griffin, S. Channa, A. Legros, W. Tabis, C. Proust, J. Neaton, L. Taillefer, J. G. Analytis, Signatures of possible surface states in TaAs. *Phys. Rev. B* **102**, 075402 (2020). doi:10.1103/PhysRevB.102.075402

34. A. A. Taskin, S. Sasaki, K. Segawa, Y. Ando, Manifestation of topological protection in transport properties of epitaxial Bi_2Se_3 thin films. *Phys. Rev. Lett.* **109**, 066803 (2012). doi:10.1103/PhysRevLett.109.066803 Medline

35. C.-I. Tsai, P.-H. Yeh, C.-Y. Wang, H.-W. Wu, U.-S. Chen, M.-Y. Lu, W.-W. Wu, L.-J. Chen, Z.-L. Wang, Cobalt silicide nanostructures: Synthesis, electron transport, and field

emission properties. *Cryst. Growth Des.* **9**, 4514–4518 (2009). [doi:10.1021/cg900531x](doi:10.1021/cg900531x)

36. J.-Z. Huang, E.-C. Chang, P.-C. Tsao, I.-C. Ni, S.-W. Li, Y.-C. Chan, S.-Y. Yang, M.-H. Lee, S.-L. Shue, M.-H. Chen, C.-I. Wu, Intercalated multilayer graphene with ultra low resistance for next-generation interconnects. *ACS Appl. Nano Mater.* **6**, 10680–10686 (2023). doi:10.1021/acsanm.3c01612

37. J. Jiang, J. H. Chu, K. Banerjee, "CMOS-compatible doped-multilayer-graphene interconnects for next-generation VLSI" in *2018 IEEE International Electron Devices Meeting (IEDM)* (IEEE, 2018), pp. 34.5.1–34.5.4; https://doi.org/10.1109/IEDM.2018.8614535.

38. S. Vaziri, V. Chen, L. Cai, Y. Jiang, M. E. Chen, R. W. Grady, X. Zheng, E. Pop, Ultrahigh doping of graphene using flame-deposited MoO_3. *IEEE Electron Device Lett.* **41**, 1592–1595 (2020). [doi:10.1109/LED.2020.3018485](doi:10.1109/LED.2020.3018485)

39. C. Fenouillet-Beranger, L. Brunet, P. Batude, L. Brevard, X. Garros, M. Cassé, J. Lacord, B. Sklenard, P. Acosta-Alba, S. Kerdilès, A. Tavernier, C. Vizioz, P. Besson, R. Gassilloud, J.-M. Pedini, J. Kanyandekwe, F. Mazen, A. Magalhaes-Lucas, C. Cavalcante, D. Bosch, M. Ribotta, V. Lapras, M. Vinet, F. Andrieu, J. Arcamone, A review of low temperature process modules leading up to the first (≤500 °C) planar FDSOI CMOS devices for 3-D sequential integration. *IEEE Trans. Electron Dev.* **68**, 3142–3148 (2021). [doi:10.1109/TED.2021.3084916](doi:10.1109/TED.2021.3084916)

40. J. Xu, M. Greenblatt, T. Emge, P. Höhn, T. Hughbanks, Y. Tian, Crystal structure, electrical transport, and magnetic properties of niobium monophosphide. *Inorg. Chem.* **35**, 845–849 (1996). [doi:10.1021/ic950826f](doi:10.1021/ic950826f) Medline

41. S. C. Hunter, F. R. N. Nabarro, R. E. Peierls, The propagation of electrons in a strained metallic lattice. *Proc. R. Soc. London. Ser. A.* **220**, 542–561 (1953).

42. K. Tanaka, T. Watanabe, An electrical resistivity study of lattice defects in deformed iron. *Jpn. J. Appl. Phys.* **11**, 1429 (1972). doi:10.1143/JJAP.11.1429

43. T. Peng, C.-B. Hua, R. Chen, Z.-R. Liu, H.-M. Huang, B. Zhou, Density-driven higher-order topological phase transitions in amorphous solids. *Phys. Rev. B* **106**, 125310 (2022). doi:10.1103/PhysRevB.106.125310

44. A. Molinari, F. Balduini, L. Rocchino, R. Wawrzyńczak, M. Sousa, H. Bui, C. Lavoie, V. Stanic, J. Jordan-Sweet, M. Hopstaken, S. Tchoumakov, S. Franca, J. Gooth, S. Fratini, A. G. Grushin, C. Zota, B. Gotsmann, H. Schmid, Disorder-induced magnetotransport anomalies in amorphous and textured $Co_{1-x}Si_x$ semimetal thin films. *ACS Appl. Electron. Mater.* **5**, 2624–2637 (2023). doi:10.1021/acsaelm.3c00095 Medline

45. H. J. Han, S. Kumar, G. Jin, X. Ji, J. L. Hart, D. J. Hynek, Q. P. Sam, V. Hasse, C. Felser, D. G. Cahill, R. Sundararaman, J. J. Cha, Topological metal MoP nanowire for interconnect. *Adv. Mater.* **35**, e2208965 (2023). doi:10.1002/adma.202208965 Medline

46. H. T. Yi, Y. N. Gartstein, V. Podzorov, Charge carrier coherence and Hall effect in organic semiconductors. *Sci. Rep.* **6**, 23650 (2016). doi:10.1038/srep23650 Medline

47. C. Wang, T. Cheng, Z. Liu, F. Liu, H. Huang, Structural amorphization-induced topological order. *Phys. Rev. Lett.* **128**, 056401 (2022). doi:10.1103/PhysRevLett.128.056401

[Medline](#)

48. A. Pyzyna, H. Tsai, M. Lofaro, L. Gignac, H. Miyazoe, R. Bruce, C. M. Breslin, M. Brink, D. Klaus, M. Guillorn, C. Lavoie, K. P. Rodbell, D.-G. Park, E. Joseph, "Resistivity of copper interconnects beyond the 7 nm node" in *2017 IEEE International Interconnect Technology Conference (IITC)* (IEEE, 2017), pp. T120–T121; https://doi.org/10.1109/VLSIT.2015.7223712.